

Three years of *Fermi* GBM Earth Occultation Monitoring: Observations of Hard X-ray/Soft Gamma-Ray Sources

Colleen A. Wilson-Hodge¹, Gary L. Case², Michael L. Cherry², James Rodi², Ascension Camero-Arranz³, Peter Jenke^{1,4}, Vandiver Chaplin⁵, Elif Beklen⁶, Mark Finger⁷, Narayan Bhat⁵, Michael S. Briggs⁵, Valerie Connaughton⁵, Jochen Greiner⁸, R. Marc Kippen⁹, Charles A. Meegan⁸, William S. Paciasas⁷, Robert Preece⁵, Andreas von Kienlin⁸

ABSTRACT

The Gamma ray Burst Monitor (GBM) on board *Fermi* has been providing continuous data to the astronomical community since 2008 August 12. In this paper we present the results of the analysis of the first three years of these continuous data using the Earth occultation technique to monitor a catalog of 209 sources. From this catalog, we detect 99 sources, including 40 low-mass X-ray binary/neutron star systems, 31 high-mass X-ray binary neutron star systems, 12 black hole binaries, 12 active galaxies, 2 other sources, plus the Crab Nebula, and the Sun. Nine of these sources are detected in the 100-300 keV band, including seven black-hole binaries, the active galaxy Cen A, and the Crab. The Crab and Cyg X-1 are also detected in the 300-500 keV band. GBM provides complementary data to other sky-monitors below 100 keV and is the only all-sky monitor above 100 keV. Up-to-date light curves for all of the catalog sources can be found at <http://heastro.phys.lsu.edu/gbm/>.

Subject headings: catalogs – gamma rays: observations – methods: data analysis – occultations – surveys – X-rays: stars

¹ZP 12 Astrophysics Office, NASA Marshall Space Flight Center, Huntsville, AL 35812

²Department of Physics and Astronomy, Louisiana State University, Baton Rouge, LA, 70803, USA

³Instituto de Ciencias del Espacio (IEEC-CSIC), Campus UAB, Torre C5, 2a planta, 08193 Barcelona, Spain

⁴NASA Postdoctoral Program Fellow

⁵University of Alabama in Huntsville, Huntsville, AL 35899, USA

⁶Physics Department, Suleyman Demirel University, 32260 Isparta, Turkey

⁷Universities Space Research Association, Huntsville, AL 35805, USA

⁸Max-Planck Institut für Extraterrestische Physik, 85748, Garching, Germany

⁹Los Alamos National Laboratory, Los Alamos, NM 87545

1. Introduction

The low energy gamma-ray/hard X-ray sky is populated largely by active X-ray binaries, active galactic nuclei, soft gamma ray repeaters, the Crab, and the Sun. *Swift*/BAT is currently monitoring the sky in the region 14 - 195 keV (Baumgartner et al. 2010). There are multiple all-sky telescopes monitoring the sky at lower energies, for example *RXTE*/ASM at 2 - 10 keV (Levine et al. 1996), and *MAXI*/GSC at 1.5 - 20 keV (Matsuoka et al. 2009). At higher energies, where instruments such as *INTEGRAL*/IBIS (Krivonos et al. 2010, 15-1000 keV) provides frequent but non-continuous observations, the most recent near-continuous all-sky catalog is that of *CGRO*/BATSE over the energy range 20 - 1800 keV (Ling et al. 2000;

Harmon et al. 2004). The BATSE survey was conducted with a set of non-imaging detectors using the Earth occultation technique (EOT, Harmon et al. 2002). The flux from an individual source is measured by detecting the step-like feature in the counting rate as the source passes into or moves out of eclipse by the Earth. Here we present a new catalog of sources over the energy range 8 - 1000 keV utilizing Earth occultation with the set of sodium iodide detectors aboard the Gamma-ray Burst Monitor (GBM) instrument (Meegan et al. 2009) on *Fermi*.

The occultation technique has been used at X-ray energies with the Moon as an occulter to detect the Crab (Bowyer et al. 1964; Fukada et al. 1975) and GX 9+1 (Davison & Morrison 1977), and BATSE demonstrated the use of Earth occultation to provide a wide-field survey of the hard X-ray/low energy gamma-ray sky over the period 1991 - 2000. Since the launch of *Fermi* on June 11, 2008 and the start of science operations on August 12, 2008, GBM has used Earth occultations to observe a pre-defined catalog of sources. Case et al. (2011a) have presented initial results, with positive identification above 100 keV of six persistent sources (the Crab, Cyg X-1, SWIFT J1753.5-0127, 1E 1740-29, Cen A, and GRS 1915+105) and two transient sources (GX 339-4 and XTE J1752-223). Wilson-Hodge et al. (2011a) used the GBM occultation measurements to demonstrate that the 15 - 100 keV flux from the Crab had decreased by approximately 7% over the time from launch through August 2010, and Camero-Arranz et al. (2012) have presented the GBM observations of the transient Be/X-ray binary system A0535+26. The present paper describes the GBM approach in detail and presents the results of the first three years of GBM Earth occultation measurements.

Sections 2 - 3 describe the GBM occultation technique. Since the method requires a comparison of the measured flux from a particular source just before occultation to the flux just after, the times of occultations must be known. In other words, a predetermined catalog of potential sources must be used. The selection of

candidate sources is described in Section 4. Systematic effects and the instrument sensitivity are discussed in Sections 5 and 6, and the results of the 3-year GBM occultation catalog are presented in Section 7.

2. GBM

The *Fermi* Gamma-ray Burst Monitor (GBM) consists of 14 detectors: 12 NaI detectors, each 12.7 cm in diameter and 1.27 cm thick (each with effective area $\sim 123 \text{ cm}^2$ at 100 keV); and two BGO detectors, 12.7 cm in diameter and 12.7 cm thick (each with effective area $\sim 120 \text{ cm}^2$ in the 0.15–2 MeV range). The NaI detectors are located on the corners of the spacecraft, with six detectors oriented such that the normals to their faces are perpendicular to the z-axis of the spacecraft (the LAT is pointed in the +z-direction), four detectors pointed at 45° from the z-axis, and 2 detectors pointed 20° off the z-axis. Together, these 12 detectors provide nearly uniform coverage of the unocculted sky in the energy range from 8 keV to 1 MeV. Typically 3-4 NaI detectors view an Earth occultation within 60 degrees of the detector normal vector. The two BGO detectors are located on opposite sides of the spacecraft and view a large part of the sky in the energy range $\sim 150 \text{ keV}$ to $\sim 40 \text{ MeV}$. It should be noted that none of the GBM detectors have direct imaging capability.

GBM has two continuous data types: CTIME data with nominal 0.256-second time resolution and 8-channel spectral resolution and CSPEC data with nominal 4.096-second time resolution and 128-channel spectral resolution. The catalog results presented in this paper use the lower-spectral resolution CTIME data for the NaI detectors. Analyses using the higher resolution CSPEC data, beyond the Crab spectrum presented in Section 7.1, and using the BGO detectors are reserved for future work.

Fermi was launched into a $i = 25.6^\circ$ inclination orbit at an altitude of 555 km. The diameter of the Earth as seen from *Fermi* is $\sim 135^\circ$, so roughly 30% of the sky is occulted by the Earth at any one time. One complete orbit of the spacecraft allows over 85% of the sky to be

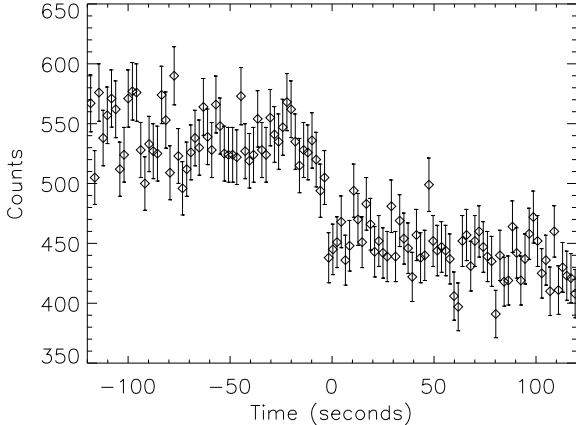


Fig. 1.— Single Crab occultation step seen in the CTIME raw counts data of a single GBM NaI detector (NaI 2) in the 12–25 keV band with 2.048-second time bins. The Crab was 4.5° from the normal to the detector. The time window is centered on the calculated occultation time for 100 keV.

observed. The precession of the orbital plane allows the entire sky to be occulted every ~ 26 days (half the precession period for the *Fermi* orbit), though the exposure is not uniform.

3. Step Fitting Technique

We have adapted the technique of Harmon et al. (2002) for GBM. This technique involves fitting a model consisting of a quadratic background plus source terms to a short (~ 4 min) window of data centered on the occultation time of the source of interest. For GBM we have incorporated the changing detector response across the fit window into our source terms. The Ling et al. (2000) approach, also used with BATSE, which involved simultaneous fits to an empirical background and numerous source terms over typically an entire day during which each source and the corresponding detector response was assumed constant, is not practical for GBM data due to the rapidly changing detector response. In addition, the Ling et al. (2000) method resulted in apparent hard tails for several weak sources that were not confirmed with other instruments (Harmon et al. 2004).

The primary difference in the implementa-

tion of the occultation technique between GBM and BATSE arises from the different pointing schemes of the respective missions. *CGRO* was three-axis stabilized for each viewing period, which typically lasted for two weeks. This meant that a source remained at a fixed orientation with respect to the detectors through an entire viewing period. In contrast, *Fermi* scans the sky by pointing in a direction 35° (August 2008–September 2009) or 50° (October 2009–present) north of the zenith for one orbit; it then rocks to 35° or 50° south for the next orbit, continuing to alternate every orbit unless the spacecraft goes into a pointed mode (which occurs rarely). In addition, the spacecraft performs a roll about the z-axis as it orbits so the solar panels face the Sun. Because the orientation of a source with respect to the GBM detectors varies as a function of time, the detector response also varies with time. A detailed instrument modeling and measurement program has been used to develop the GBM instrument response as a function of direction (Hoover et al. 2008; Bissaldi et al. 2009; Meegan et al. 2009) and has produced a database of detector responses for each detector at 272 spacecraft positions. For the occultation analysis we interpolated this database to produce matrices for the same 272 positions using 137 photon input energies (from 5 keV to 50 MeV) and using 3-year average CTIME channel energy edges for each detector and for each of the 8 CTIME channel energy edges (approximately < 12 , 12–25, 25–50, 50–100, 100–300, 300–500, 500–1000, > 1000 keV). Custom energy matrices can be constructed using CSPEC data at full resolution, or in combinations which provide fine resolution in the energy band of interest while maintaining a small number of output channels in the response matrix. In the individual step fitting, the spacecraft position of each source in the fit is computed as a function of time. A new response matrix is interpolated from our database using its three nearest neighbors every time the spacecraft moves by $\sim 2^\circ$.

Before any sources are fitted, good time intervals (GTIs) of GBM data are defined. The GTI intervals from the CTIME data files are

shortened by 10 s to remove transient events due to GBM high voltage turn-on and turn-off. A spline model is fitted to the 12-25 keV CTIME data to eliminate large background deviations, typically on ~ 100 s time scales, due to South Atlantic Anomaly entries and exits, bright solar flares, gamma-ray bursts, and other brief bright events from the GTIs.

Mission averaged energy channel edges are used in the detector response matrices. Gain variations in individual detectors due to temperatures or other effects are controlled using an on-board automatic gain control to keep the 511 keV line in a particular on-board channel (one of 4096). The maximum temperature variation observed to date was ~ 4.35 C in December 2008, which corresponds to a gain change of 1.36%, which is negligible. Because scintillators are massive compared to semiconductor detectors, temperature changes have much less impact for GBM than for other X-ray missions using semiconductors or CCDs.

For each day, the occultation times for each source in the catalog are calculated using the known spacecraft positions. The time of each occultation step, t_0 , is taken to be the time for which the transmission of a 100 keV gamma ray through the atmospheric column is 50%. A fit window of data, lasting 240 seconds and centered on t_0 is used for each step. The time at which the atmospheric transmission reaches 50% is energy dependent, with lower energies absorbed at lower atmospheric densities so that a setting step will occur earlier than at higher energies (see Fig. 1). This energy dependence is accounted for in the calculation of the atmospheric transmission function $T(E_{ph}, t)$, given by

$$T(E_{ph}, t) = \exp[-\mu(E_{ph})A(h(t))] \quad (1)$$

where $\mu(E_{ph})$ is the mass attenuation coefficient of gamma rays at photon energy E_{ph} in air¹ and $A(h(t))$ is the air mass along the line of sight at a given altitude $h(t)$ based on the US Standard Atmosphere (1976). This requires instantaneous knowledge of the spacecraft

position, the direction to the source of interest as seen from the spacecraft, and a model of the Earth that includes its oblateness. Changes in chemical content with altitude and changes in the atmospheric height with solar activity are not included in the current atmospheric model. Atmospheric density measurements with sounding rockets (Quiroz 1961) show that at mid-latitudes the standard deviation of the density varies from 4% at 30 km to about 20% at 60km and above. To estimate the effect of these variations on our Earth occultation flux measurements, we varied the air mass $A(h(t))$ by 10% and 50% in fits to the Crab Nebula. This resulted in changes to the daily Crab flux measurements of $< 2\%$ in the four bands spanning 12-300 keV. Therefore we ignore the effects of atmospheric variations in our model.

Measuring the flux from the source of interest requires fitting a model to the count rate data. For each detector viewing the source of interest within 60° from the detector normal, within the fit time window, the observed count rate $r(t, E_{ch})$ at time t in each energy channel E_{ch} is modeled as

$$r(t, E_{ch}) = b_0(E_{ch}) + b_1(E_{ch}) * (t - t_0) + b_2(E_{ch}) * (t - t_0)^2 + \sum_{i=1}^n a_i(E_{ch}) * S_i(t, E_{ch}) \quad (2)$$

where $b_0(E_{ch})$, $b_1(E_{ch})$, and $b_2(E_{ch})$ are quadratic background coefficients, $S_i(t, E_{ch})$ are source models summed for the source of interest and all interfering sources included in the fit, and $a_i(E_{ch})$ are the fitted scale factors for each source model. The background is typically smooth and adequately fitted by the second-order polynomial within the 240 second fit window. The source count rate models are given by

$$S(t, E_{ch}) = R(E_{ph}, E_{ch}, t) T(E_{ph}, t) \int_{E_{ph}} f(E_{ph}) dE_{ph} \quad (3)$$

where E_{ph} are photon energies, matching the input side of the time-dependent detector response matrix, $R(E_{ph}, E_{ch}, t)$. The assumed energy spectrum for each source integrated over

¹<http://physics.nist.gov/PhysRefData/XrayMassCoef/ComTab/air.html>

each photon energy bin, $\int_{E_{ph}} f(E_{ph}) dE_{ph}$, is combined with the atmospheric transmission $T(E_{ph}, t)$ and convolved with the detector response $R(E_{ph}, E_{ch}, t)$ to compute the predicted count rate in each energy channel E_{ch} at time t .

Each energy channel and each detector is fitted independently. For each source term a scaling factor $a_i(E_{ch}, t)$ is fitted, along with the quadratic background coefficients. When multiple detectors are included in the fit, the weighted mean for the scaling factor of the source of interest is computed for each energy channel. The mean scaling factor is then multiplied by the predicted flux in each energy channel to obtain flux measurements for the source of interest.

Ideally, each occultation measurement would include the effects of every other source in the sky, but this is not practical to implement. We have adopted a top-down iterative approach for treating interfering sources. Following Harmon et al. (2004), we have implemented a flare database consisting of times when sources are active and broad levels of activity. For our first iteration, we have used public *Swift*/BAT transient monitor data to populate our flare database. Later iterations will incorporate results from GBM and from the *Swift*/BAT survey over a wider energy range. Currently any source that has a 15–50 keV flux of 50 mCrab or larger in *Swift*/BAT that persists for at least a few days is included in the database. On any particular day in the flare database, sources are grouped into three classes: (1) > 500 mCrab, (2) 150–500 mCrab, or (3) 50–150 mCrab. A source’s class changes in the database whenever the flux drops or rises into the next class. If a source changes flux quickly within a single day, the brightest class for that day is retained. Identical source classes are used in the source catalog for persistent sources. Sources in these classes are included as interfering sources if they undergo Earth occultation in the fit window and if they are within 90° , 60° , or 40° of the detector normal for classes 1, 2, and 3, respectively. Fainter sources are not currently considered in occultation fits except when they are the source of interest. This paper reports results from our

first iteration, in which we treat the brightest sources first to optimize interfering source inclusion. Our code is flexible, so additional source classes can be added if needed in the future to support analysis of fainter sources. In addition to the flare database, we maintain an eclipse database, containing ephemerides for ten eclipsing sources. When any of these ten sources are in eclipse, they are not included as interfering sources in step fitting, regardless of their levels set in the catalog or flare database.

At lower energies, especially below about 50 keV, the Sun is a special case of a bright interfering source. We maintain a solar flare database, built from Solar event reports of Geostationary Operational Environment Satellites (GOES) data obtained from the National Oceanic and Atmospheric Administration (NOAA) Space Weather Prediction Center². In our solar flare database we use classes for the flares, based upon the peak GOES flux in the flare: (1) Class M or X flares, included as an interfering source if the Sun is within 90° of the detector normal, (2) Class C flares, included as an interfering source if the Sun is within 60° of the detector normal, and (3) Class B flares, included as an interfering source if the Sun is within 40° of the detector normal. Since the Sun moves with respect to other sources in the sky, the Sun’s position is initially calculated for the center of the day. This position is used to find fit windows that include the Sun. At the time the data are fitted, the Sun position at the time of the fit window is calculated to correctly compute the atmospheric transmission. Small errors in the timing of Sun steps still exist, because the Sun is not a point source and the position of the center of the Solar disk is used. Data containing X or M class flares are usually filtered out from the GTIs before steps are fitted, so only C class and fainter flares are typically included as interfering sources.

Once the steps are fitted, source count rates and errors for the source of interest are written to a Flexible Image Transport System (FITS)

²<http://www.swpc.noaa.gov/>

file for each detector along with other information about the fit including the flux and error measurement in each energy channel, the step times, sources included in the fit, detectors, and angles to the source of interest at the time of occultation. Light curves and energy spectra are extracted from these files. Light curves used in this catalog paper have been post-filtered using the following criteria: (1) occultation steps are excluded if the source of interest occults within 8 seconds of a bright source, if the occultation transition lasts longer than 20 seconds, or if the spacecraft is rapidly slewing with a spin rate > 0.004 rad/s. (2) individual steps that are $> 10\sigma$ or $> 3.5\sigma$ from the mean are filtered out for sources with intensities reaching 150-500 mCrab or < 150 mCrab, respectively. Outliers for sources that reach fluxes > 500 mCrab are not filtered out to avoid discarding real flares. (3) occultation steps during solar flares are also discarded.

4. Source Catalog Selection

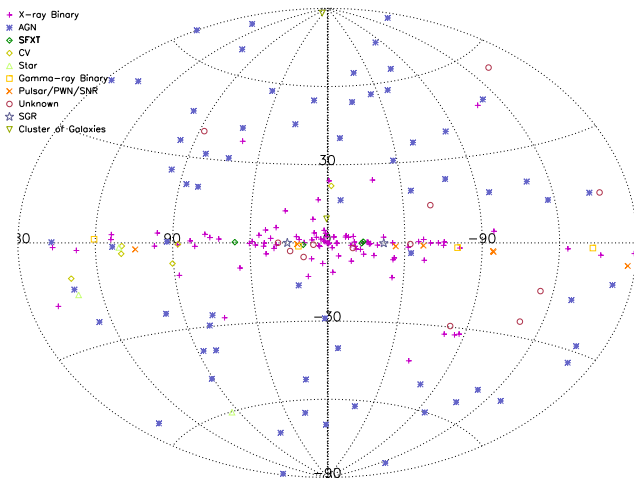


Fig. 2.— Sky map in equatorial coordinates showing the sources included in the GBM occultation catalog.

As described in the previous section, the Earth occultation technique being used with GBM is catalog-driven meaning that only those sources included in the catalog are measured. Because GBM is sensitive to lower energies than

BATSE, the occultation catalog was expanded to include sources and even source classes that were undetected with BATSE but seen to be bright in pointed X-ray instruments such as *INTEGRAL*, *MAXI*, *Swift*/BAT, or *RXTE*/ASM. In addition, extragalactic sources with two spectral components that are shown to be bright in the *Fermi*/LAT and to exhibit bright flares on time-scales of days or weeks were viewed as viable candidates for our catalog, though their quiescent levels would typically be faint. To be as complete as possible, we adopted an iterative approach, first selecting sources for the catalog that were detected with BATSE using Earth occultation (Harmon et al. 2004) plus bright sources (> 50 mCrab) detected with *Swift*/BAT, *MAXI*, or *INTEGRAL*/IBIS. This initial catalog was then expanded by adding 14 sources detected using GBM Earth occultation imaging (Rodi et al. 2011). To prepare for this catalog paper, we did a more thorough effort of source selection, selecting sources detected above ~ 10 mCrab with *Swift*/BAT in the transient monitor³ or in the *Swift*/BAT 58 month survey⁴, or detected above ~ 20 mCrab in public light curves from either *RXTE*/ASM⁵ or *MAXI*⁶. To further broaden our inclusion of source types, we also explored cataclysmic variables (CVs) detected with *INTEGRAL*, Supergiant Fast X-ray Transients (SFXTs) detected with *INTEGRAL* and *Swift*/BAT, pulsar wind nebulae and gamma-ray binaries detected with *Fermi*/LAT (Abdo et al. 2011). For active galaxies (AGN), we selected sources detected with the Oriented Scintillation Spectrometer Experiment (OSSE) on CGRO and sources detected in the LAT 2-year AGN catalog (Ackermann et al. 2011a) that met the following criteria: (1) $\gtrsim 10^\circ$ from the galactic plane, (2) flagged as in the LAT Clean sample, (3) classified as either a BL Lac with a High Synchrotron Peak (HSP) or classified as a Flat Spectrum Radio Quiet source (FSRQ) with a

³<http://swift.gsfc.nasa.gov/docs/swift/results/transients/>

⁴<http://swift.gsfc.nasa.gov/docs/swift/results/bs58mon/>

⁵<http://xte.mit.edu/>

⁶<http://maxi.riken.jp/top/>

Low Synchrotron peak. The reasoning is that for the BL Lacs, the GBM energy range will sample the fall-off of the νF_ν synchrotron peak while the LAT is sampling the IC peak, and for FSRQs, the GBM band will sample the rise of the IC peak while the LAT samples the fall of the IC peak (assuming Leptonic processes), making these sources more likely to be detectable with GBM, and (4) a test statistic of > 600 in the full LAT energy range in the 2-year catalog, to limit this initial sample to the brightest LAT sources. These selections resulted in a catalog, shown in Figure 2, containing 209 sources, including 71 active galaxies (AGN), 52 low-mass X-ray binary/neutron star (LMXB/NS) systems, 40 high-mass x-ray binary/neutron star (HMXB/NS) systems (including 5 supergiant fast X-ray transients (SFXT)), 19 black hole candidates (BHC), 8 pulsars (PSR)/pulsar wind nebulae (PWN)/supernova remnants (SNR), 6 CVs, 4 gamma ray binaries, 2 galaxy clusters, 3 stars including the Sun, 2 SGRs, 1 globular cluster, and 1 tidal disruption event (TDE).

5. Systematic Effects

5.1. Description of known effects and Mitigation Strategies

From our experience using the Earth occultation technique with BATSE and with GBM, we have identified the following systematic effects that affect Earth occultation flux measurements: (1) accuracy of the assumed source spectra, (2) large variations in the background, (3) duration of the occultation transition, (4) inaccuracies in the detector response matrices, (5) occultation limb geometry, and (6) nearby sources. In this section we describe our mitigation strategies and our efforts to reduce, account for, or quantify these effects.

We explored the effects of incorrectly assumed source spectra using multiple runs of the Earth occultation software for the Crab assuming (1) a canonical spectrum (Toor & Seward 1974), (2) an exponential cut-off spectrum (with a cutoff energy of 30 keV and e-folding energy of 13.6 keV), (3) the exponential cutoff spec-

trum plus a 1 mCrab power law with photon index $= -2$, (4) a power law with a photon index $= -3$, and (5) a hard power law with photon index $= -1$. The measured count rates in each step were consistent within errors, indicating that the fitting process is robust, and in particular that the treatment of interfering source steps in the fit window is little affected by the assumed source spectrum. Further we found that the statistical significance of the average flux in each energy channel was consistent for all five assumed spectra. The flux values showed systematic effects, however. For the “incorrect” spectra, models 3 and 4, fluxes were consistent with the canonical values within 5-10%, while model 2, which changes rapidly at higher energies, and the very hard model 5 showed large flux deviations. This test was repeated using models 2-5 for Vela X-1 and the results were the same as for the Crab. From 12 to 100 keV, where Vela X-1 is detected with GBM, count rates and significances were consistent for all models. Model 2 is based upon Vela X-1 BATSE data (Bildsten et al. 1997). Models 3 and 4 fluxes were within 5-10% of model 2 fluxes, while model 5 again showed large deviations. Therefore, the assumed spectrum does not appear to significantly affect detection significance or fits to other sources. Its primary impact is on the reported flux values. For this paper, we have done an extensive literature search to obtain the best published spectra for the sources in our catalog. Where appropriate spectra in our energy range are not available, these tests show that model 4, a power law with photon index $= -3$, gives fluxes consistent to 5-10% with expected models for both a harder source (Crab) and a softer source (Vela X-1). We have adopted model 4 as a generic flux model for sources lacking spectra in the GBM energy range or for sources with rapidly changing spectra. As described in Section 7.3 we have also compared our results with *Swift*/BAT in overlapping energy bands, where we generally found good agreement.

Because the background and sources are fit simultaneously, variations in the background that cannot be fitted with a quadratic function will

be absorbed into the source terms and can potentially affect source measurements. For all of these background effects, our mitigation strategy is to exclude these data from the occultation flux measurements. We performed an investigation where we examined the CTIME count rates in the 12-25 keV band for times when we saw large outliers for Earth occultation flux measurements for the Crab, Cen A, and a few additional sources. These outliers frequently corresponded to times with large variations in the background, such as large slopes due to SAA entry or exit, bright (X or M class) solar flares, or intervals where *Fermi* is slewing or rotating rapidly. To mitigate these effects, we pre-filter the data, fitting a spline model to the 12-25 keV rates and excluding intervals with large deviations from this smooth model from the GTIs, so that these data are not used for occultation step fitting. This pre-filtering eliminates SAA entries and exits and bright solar flares from further analysis and is believed effective in eliminating similar effects that we have not yet identified. The spacecraft spin-rate is given by

$$(wsj_1^2 + wsj_2^2 + wsj_3^2)^{1/2} \quad (4)$$

where wsj_i are the instantaneous angular velocity components for the spacecraft, available in public spacecraft position history files from the *Fermi* Science Support Center⁷. For this catalog, fit windows with spin-rates $> 4 \times 10^{-3}$ rad s⁻¹ were flagged and excluded from further analysis. This is an adjustable parameter in the occultation software, which is currently set conservatively to eliminate steps where the high-spin rate adversely affects the fitting.

An Earth occultation has a finite transition time due to the effect of absorption in the Earth's atmosphere. Since the orbital period of the spacecraft is ~ 96 minutes, the individual occultation steps last for $\sim 8/\cos\beta$ seconds, where β is defined as the elevation angle of the source being occulted with respect to the plane of the *Fermi* orbit. Since the *Fermi* orbit has an inclination of 25.6° , sources with declinations

larger than $\approx \pm 40^\circ$ undergo intervals where they are no longer occulted. When $\beta \sim 66^\circ$ these sources are still being occulted, but the occultations are very broad, lasting > 20 seconds. Our analysis has shown that our flux measurements become unreliable if the transition lasts longer than about 20 seconds, so we flag these long duration steps and exclude them from further analysis.

The most noticeable systematic effect arising from the detector response matrices are solar panel occultations of sources. In the mass model for *Fermi* used to derive the responses, the solar panels are included at a fixed orientation, with the top rotated in the +X direction by 20° (where 0° is vertical alignment in the Y-Z plane). The true solar panel orientation is not fixed, and may block a source, an effect that is particularly severe at low energies. The discrepancy between the modeled response assuming a fixed solar panel orientation and the true response to the source yields predicted blockages that do not occur or real blockages that are not predicted. To account for either of these issues, we have defined potential solar panel blockage regions in spacecraft coordinates for each detector based upon the full-range of motion of the solar panels. If the source of interest or an interfering source is in that region in spacecraft coordinates, that detector is excluded from occultation step fitting. Typically this blockage only occurs in 1-2 NaI detectors, and a flux measurement based on unblocked detectors is calculated where possible. In addition to the solar panel blockage regions, we have identified two small regions where Crab, Sco X-1, or Cyg X-1 occultations were obviously blocked in NaI 11, based upon low-flux measurements only in NaI 11. These blockage regions are believed to be due to small structures on the spacecraft that were not included in the response model, so NaI 11 data is excluded from fits if any sources included in the fit are in this region. Photopeak efficiencies measured during the *Fermi* source survey (with the solar panels folded) agree with the mass model simulations to within 5% rms for detectors with source angles $< 90^\circ$ confirming the

⁷<http://fermi.gsfc.nasa.gov/ssc/data/access/>

accuracy of the responses for larger spacecraft structures (Meegan et al. 2009).

Every ~ 52 days, the *Fermi* orbit precesses so that the Earth occultation limb geometry (i.e. the projection of the Earth’s limb on the sky) repeats at this period. For a particular geometry, Earth occultation flux measurements may be systematically low or high due to unmodelled sources or non-point source backgrounds such as galactic ridge emission. These systematic effects can be very difficult to identify. To mitigate these effects, we use *Swift*/BAT data to populate a flare database listing times and brightness levels for potentially interfering sources. This database is updated with current flares and if past flares were missed, they can be added and the occultation code rerun. Using Earth occultation imaging (Rodi et al. 2011), combined with existing catalogs of known source locations, we identified 14 sources detected with $> 10\sigma$ significance that were not initially included in the Earth occultation catalog. These sources were added to the catalog. The catalog and flare database continue to be iteratively updated to extract our best results.

Nearby sources, especially bright or highly variable sources, can make occultation measurements very difficult. If two occultation steps occur within 8 seconds of each other, the step fitting breaks down, so we automatically flag these steps and exclude them from further analysis. The angular resolution of the occultation technique is $360^\circ \times \Delta t/P$ where Δt is the occultation duration and P is *Fermi*’s orbital period (~ 96 minutes). The occultation duration Δt varies as $8/\cos(\beta)$ seconds, where β is the elevation angle between the source and the orbital plane of *Fermi*. The angular resolution ranges from $\sim 0.5^\circ$ at $\beta = 0^\circ$ to $\sim 1.25^\circ$ at $\beta = 66^\circ$. When $\beta > 66^\circ$, occultations no longer occur. Some remaining nearby source effects are relatively easy to identify, e.g the bright outburst of A0535+26 in December 2009 that is visible in the raw Crab light curve. When these effects can be easily identified, we manually flag these data and exclude them from further analysis. However in crowded regions such as the galactic

center, such simple approaches can break down, resulting in a flux measurement that is the sum of multiple sources within $\sim 1^\circ$, if uncatalogued sources become active.

In the next section, we describe our analysis of “blank” sky positions (where no source is present) where we quantify observed systematic effects.

5.2. “Ghost” source analysis

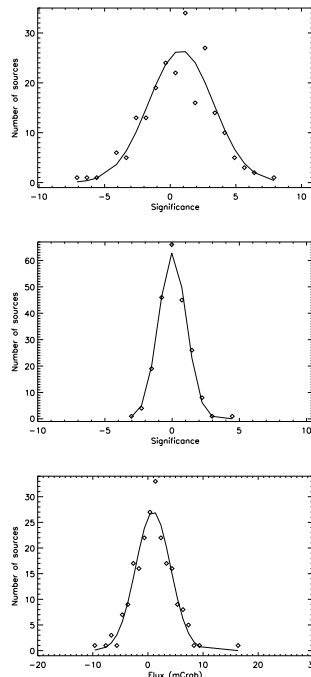


Fig. 3.— Top: Flux significance for the “ghost” sources in the 12-25 keV band before systematic error correction. The standard deviation is 2.46. Center: Flux significance for the “ghost” sources in the 12-25 keV band after systematic error correction. The new standard deviation is 1.02. Bottom: The distribution of “ghost” source fluxes in the 12-25 keV band has a mean flux of 0.94 mCrab and a standard deviation of 3.15 mCrab.

To examine the remaining systematic effects, 3-year light curves were selected from ~ 512 “ghost” sources run through the occultation software in conjunction with GBM imaging analyses (Rodi et al. 2011). The initial list was reduced by excluding any “ghost” sources

within $\pm 10^\circ$ in longitude and latitude of the galactic center. Any “ghost” sources within 2° of a source in the GBM catalog were also removed, resulting in a sample of about 200 “ghost” sources distributed over the whole sky. We investigated scatter plots of various combinations of parameters including location on the sky, flux, flux significance, flux statistical error, and flux standard deviation in all eight energy bands.

These distributions were used to estimate overall systematic errors on the flux measurements. Since no source was expected at these locations, the distribution of the flux significance in each channel is expected to be centered on zero with a standard distribution of 1.0. The distributions were centered on zero, but were broader than expected. In the flux distributions, the expected standard deviation gives a measure of the total error. To find the systematic error, we used the significance distributions to calculate a scale factor for each energy band by dividing the expected standard deviation (1.0) by the measured standard deviation. These scale factors were then multiplied by the measured flux distribution standard deviation to calculate the expected statistical flux standard deviation for each energy band. From there, we calculated the difference between the squares of the measured flux standard deviation and the calculated statistical standard deviation to get the square of the systematic standard deviation. This method gives systematic errors shown in Table 1. These errors added in quadrature to the statistical errors for the “ghost” sources result in standard deviations of ~ 1 for the flux significance distributions. As an example of the process, Figure 3 shows the flux significance distributions, before

and after systematic error correction, and the flux distribution for the 12-25 keV band.

6. Sensitivity

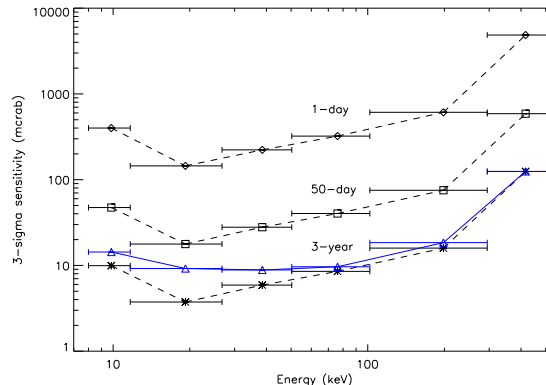


Fig. 4.— Estimated $3\text{-}\sigma$ sensitivities for the GBM Earth occultation technique from 8-500 keV. Statistical estimates are shown for 1-day (diamonds), 50-day (squares), and 3-year (asterisks) intervals. Systematic errors from Table 1 have been added in quadrature to the 3-year statistical errors and are plotted as triangles connected with solid lines.

Calculating the sensitivity for the Earth occultation technique is made challenging by the constantly changing spacecraft source geometry, detector response, and the constantly changing hard X-ray sky. To estimate the statistical sensitivity of the technique, we used four detected sources, the Crab (a galactic source in a relatively uncrowded region), Centaurus A (an active galaxy at high galactic latitude and high declination to account for steps lost when the source was at high beta angles), NGC 4151 (another active galaxy at high galactic latitude and moderate declination), and GRS 1915+105 (a persistent black hole system near but not at the galactic center). For each of these sources, 1-day, 50-day, and 3-year average measured fluxes and statistical errors were computed. The average error in each energy channel for each source was then computed. The approximate statistical sensitivity for each source was computed as three times the average error in mCrab units. For the three year averages only the systematic

Table 1: Systematic error estimates for GBM Earth occultation analysis

Energy band (keV)	Systematic error (mCrab)
8-12	3.4
12-25	2.8
25-50	2.2
50-100	1.5
100-300	3.1
300-500	3.4

errors from Table 1 were added in quadrature. Figure 4 shows the estimated sensitivities, averaged for the four sources.

As a check of our sensitivity estimate, we followed the Harmon et al. (2002) sensitivity estimate for BATSE where they used fitted count rates and count rate errors to estimate the flux sensitivity, specifically

$$F_{\min} = \delta r_{\text{Crab}} \frac{N_{\sigma} F_{\text{Crab}}}{r_{\text{Crab}}} \quad (5)$$

where F_{\min} is the minimum detectable flux for N_{σ} significance, δr_{Crab} is the uncertainty on the fitted Crab count rate r_{Crab} , and F_{Crab} is the Crab Nebula flux. To implement this method, we computed the weighted mean count rate for each occultation step across the detectors in each fit and then computed weighted mean count rates with time. The 3-year sensitivity estimate from this method was consistent within 1-2% with our simple approach using the flux errors. Based on the way the GBM fluxes are computed, using the weighted average of the scale factors between detectors, one would expect these two approaches to be approximately equivalent.

7. Results

7.1. Fitting the Crab energy spectrum

Spectral analysis with the EOT requires more than the eight energy channels available with CTIME data. However the current EOT software is designed for 8-channel data. The simplest approach to increasing the number of energy channels is to combine CSPEC channels to create a custom 8-channel CSPEC data set. Re-running the EOT code with different custom 8-channel CSPEC data sets results in a final spectrum with a multiple of eight channels. We can customize the energy bins (to within the constraints of CSPEC energy edges) to the source of interest. The resulting rates calculated from the step fits for each detector are then binned according to the position of the source in the space-craft coordinate frame. A detector response is then generated for each position bin.

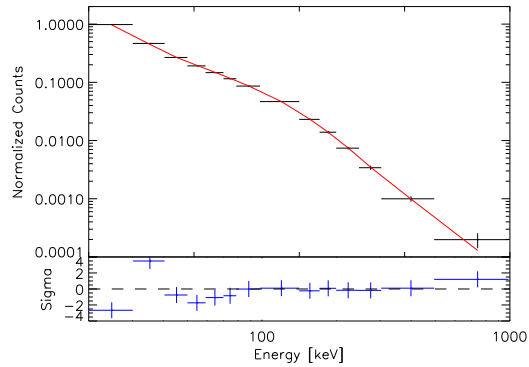


Fig. 5.— Fit to the Crab spectrum using 14,620 Earth occultation steps, approximately 1.7 Ms of on source time, and 42 position bins. An average spectrum, averaged over the 69 spectra simultaneously fit, and the fit model are shown. The best fit broken power-law model had a lower photon index of 2.057 ± 0.01 , break energy of 98 ± 9 keV, and an upper photon index of 2.36 ± 0.05 .

The spectra and responses for the position bins are fit to a photon model in XSPEC. Due to the limited exposure time in individual occultation steps for a source, spectral analysis with EOT will usually be performed with time averaged spectra. To demonstrate this technique and to add confidence in the EOT we have performed this analysis using occultation rates calculated from observations of the Crab. Since the pulsar and the nebula can not be distinguished with the EOT we expect an averaged spectrum for the pulsar and nebula. Two different runs with custom CSPEC data were used to create the spectrum; a low energy run with bins: (10-15 keV, 15-20 keV, 20-30 keV, 30-40 keV, 40-50 keV, 50-60 keV, 60-70 keV, 70-80 keV), and a high energy run with bins: (80-100 keV, 100-140 keV, 140-170 keV, 170-200 keV, 200-250 keV, 250-300 keV, 300-500 keV, 500-1000 keV). The data used are for the entire three year interval from 2008 August 12 to 2011 August 11. Position bins with fewer than 80 steps were excluded from the analysis. Each position bin was $6^\circ \times 8^\circ$. A total of 42 position bins were used in this analysis. These bins contained a total of 14,620 steps for

an exposure time of approximately 1.7Ms (assuming ~ 120 s of exposure per step). Each sky bin typically was favorably viewed by 1-4 detectors (typically one detector), resulting in a total of 10 different NaI detectors. The sky bins and detectors resulted in 69 spectra, each with 14 energy bins from 20-1000.0 keV, that were simultaneously fitted with a broken power-law model in XSPEC. Below 19.4 keV, the data contained considerable scatter that reduced the quality of the fit. Due to the numerous spectra simultaneously fit, an average spectrum and the fit model are shown in Figure 5. A broken power-law with a lower index of 2.057 ± 0.009 , a break energy of 98 ± 9 keV, and an upper index of 2.36 ± 0.05 fit the data with $\chi^2 = 1280.44$ with 962 degrees of freedom ($\chi^2_\nu = 1.33$). This result is consistent with Jourdain & Roques (2009) who fit the *INTEGRAL*/SPI Crab data to a broken power-law with an index of 2.07 ± 0.01 below 100 keV and 2.23 ± 0.05 above 100 keV.

7.2. 3-year catalog

Tables 2, 3, and 4 contain the three year (August 12, 2008 - August 11, 2011) GBM Occultation catalog results for 209 sources. Table 2 lists detected sources (as defined below), Table 3 lists marginal detections ($3 - 5\sigma$), and Table 4 lists 3σ upper-limits for non-detected sources in the catalog. The average flux in mCrabs for each source over three years is listed for 12-25 keV, 25-50 keV, 50-100 keV and 100-300 keV energy bands as well as the significance in the 12-50 keV and 12-300 keV energy bands. Downloadable up to date postscript plots and plain text files of the 4-band light curves for all sources are available from our website <http://heastro.phys.lsu.edu/gbm/>. All errors include statistical and the estimated systematic errors given in Table 1. If the significance for any source in any of the above energy bands equals or exceeds 5 sigma or the source is detected in the transient search (section 7.4) or with the orbit period folding technique (section 7.5) then the information on that source is listed in Table 2 and the source is considered a detection. In this catalog, 99 sources are con-

sidered detections. Detection categories, column four in Table 2-4, are defined as: A = $> 5\sigma$ in any of the bands 12-25, 25-50, 50-100, 100-300, 12-50, or 12-300 keV, B= $3-5\sigma$ in those bands, N = non-detection = $> -3\sigma$ and $< +3\sigma$ in those bands, I = indeterminate $< -3\sigma$ in any of the bands, which is indicative of source interference problems, T = transient detected in the transient search (section 7.4), P = detected in the orbit period folding (section 7.5). The most numerous source classification detected in categories A and/or T are LMXB/NS (40 sources) followed by HMXB/NS (31 sources), including one SFXT. Sample HMXB/NS and LMXB/NS light curves are shown in Figure 6. The 12 black hole candidates (BHC) are the next most numerous binary detected with 7 BHCs being detected above 100 keV and with Cyg X-1 detected up to and above 300 keV. We also have 12 AGNs detected, most of which are Seyfert 2 galaxies (NGC 1275, NGC 2110, NGC 4388, Cen A, NGC 5252, Circinus Galaxy, NGC 5506) with two Seyfert 1 galaxies (NGC 4151, IC 4329A), a radio galaxy (IGR J21247+5058), and two quasars (3C 273 and 3C 454.3), all of which are also seen with the Fermi/LAT. Furthermore, Cen A is detected up to and above 100 keV. The Crab pulsar together with its wind nebula is our second most significant source behind the LMXB/NS Sco X-1. The Ophiuchus Cluster is also detected as category A but only in the 12-25 keV band. The Sun (also discussed in Section 3) is also detected in the 3-year average to 96 sigma in the 8-12 keV band and numerous flares are detected to >10 sigma up to ~ 50 keV using the Earth Occultation Technique. GBM detects solar flares in triggered observations up to ~ 8 MeV with detections to higher energies in *Fermi*/LAT (Ackermann et al. 2011b).

Category B ($3-5\sigma$) contains 23 sources, listed in Table 3, including six AGN, three BL Lac objects (MRK421, H 1517+656, B2 1732+38A), two Seyfert 1 (NGC3783 and TXS 1700+685) and one Seyfert 2 (MCG-05-23-016), four LMXB/NS (4U1323-62, GRS1724-308, SAXJ1806.5-2115, 4U2127+119), five HMXB/NS (3A0114+650, IGRJ16418-4532, SAX J1818.6-

1703,XTEJ1855-026, 4U2206+54), two PSR/PWN (MSH 15-52, Vela-X), one CV (GK Per), the Vela pulsar, one BHC (LMX X-3), the Coma Cluster, a gamma ray binary (1FGLJ1018.6-5856), and a supernova remnant (Cas A). These sources may become detectable above 5σ with additional observation time.

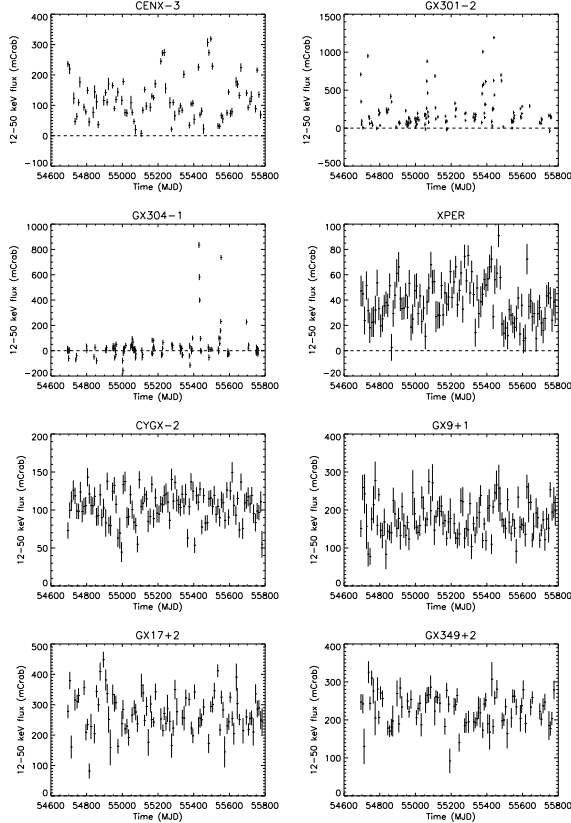


Fig. 6.— Sample 12-50 keV GBM light curves for four HMXB/NS systems containing accreting pulsars and four LMXB/NS systems, including two X-ray bursters, Cygnus X-2 and GX 17+2. Points plotted are 2-day average fluxes for GX 301-2 and GX 304-1 and are 10-day averages for the other six objects.

The Earth occultation technique allows us to do important monitoring of the hard X-ray/low energy gamma-ray sky. This is especially important as GBM is the only instrument that can provide nearly continuous monitoring of sources above 100 keV. For example, Figures 7 and 8 show that Cyg X-1 has made two hard-to-soft state transitions between 2010 July and 2011 Decem-

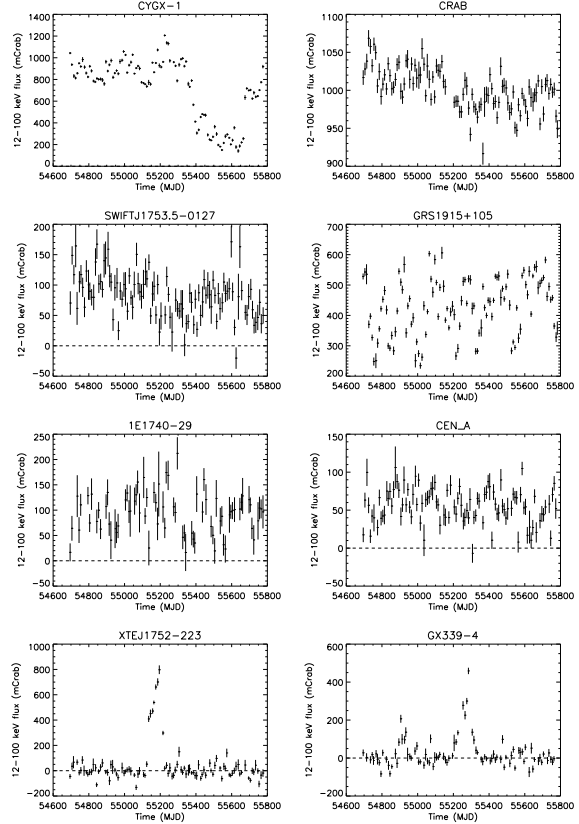


Fig. 7.— GBM lower energy (12-100 keV) light curves for the eight objects detected above 100 keV in this 3-year catalog. Each data point is a 10-day average flux. The dashed line denotes zero flux.

ber (Negoro et al. 2010; Rushton et al. 2010; Wilson-Hodge & Case 2010; Negoro et al. 2011; Grinberg et al. 2011; Case et al. 2011b). We have used the GBM spectral extraction tools (see Section 7.1) to generate spectra in the 10-400 keV energy range for the hard and soft states. We were able to verify that Cyg X-1 was in an unusually hard state from at least the beginning of the *Fermi* mission up to the first hard-to-soft transition (Nowak et al. 2011; Case et al. 2011d). After Cyg X-1 made the transition back to the hard state, the spectrum more closely resembled the typical hard state spectrum. Cyg X-1 returned to the hard state in 2011 December following a second hard-to-soft transition, and we were able to alert the community that the transition back to the hard state had occurred (Case et al. 2011c). The

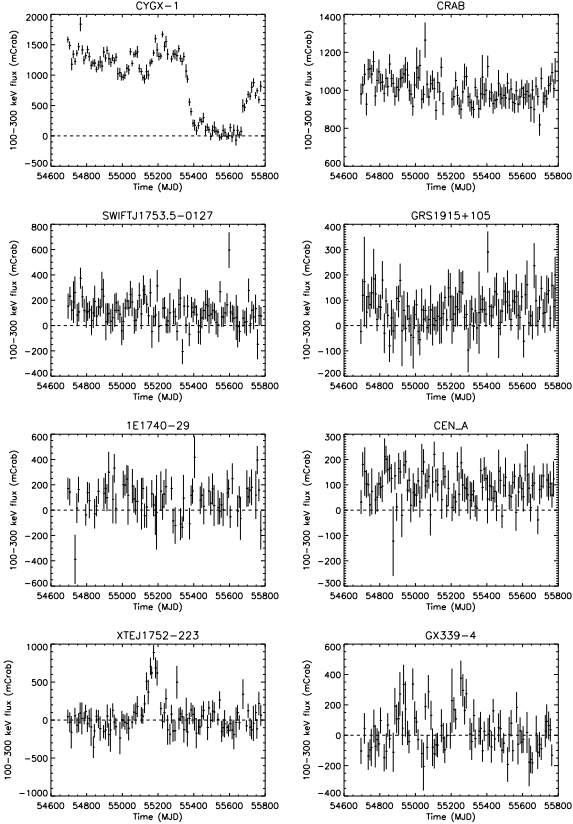


Fig. 8.— GBM higher energy (100-300 keV) light curves for the eight objects detected above 100 keV in this 3-year catalog. Each data point is a 10-day average flux. The dashed line denotes zero flux.

spectrum in the hard state is again similar to the canonical hard state spectrum. A more detailed study of Cyg X-1 will be published soon (Case et al. 2012).

In 2010 we made the surprising discovery using GBM Earth occultation data that the Crab Nebula flux had declined by 7% in the 15-100 keV band over the first two years of the *Fermi* mission, and confirmed this discovery with *INTEGRAL*, *RXTE*, and *Swift* (Wilson-Hodge et al. 2011a). In the third year, the GBM data showed that this decline has leveled off and appears to have started a gradual recovery, so far less dramatic than the two-year decline (See Figures 7 & 8 and Wilson-Hodge et al. (2011b))

Analysis of the first two years of data look-

ing only above 100 keV resulted in 8 sources (6 persistent, 2 transient) detected in the 100–300 keV band and 2 sources detected above 300 keV (Case et al. 2011a). The persistent sources detected are the Crab, the BHCs Cyg X-1, SWIFT J1753.5-0127, GRS 1915+105, and 1E 1740-29, and the AGN Cen A. The transient sources detected are the BHCs XTE J1752-223 and GX 339-4. These results were generated using our previous version of the occultation code with a smaller input catalog. The detection threshold was 7σ and no systematic errors were included. Using three years of data with the catalog presented here, Figures 7 and 8 show that all 8 of the sources are detected at greater than 5σ including the systematic errors (see Table 2). The Crab and Cyg X-1 remain the only two sources detected above 300 keV, with 3-year average fluxes of 1000 ± 40 mCrab (25σ) and 500 ± 50 mCrab (10σ), respectively.

Our imaging analysis (Rodi et al. 2011) has also indicated the presence of a significant source in the 100-300 keV band near the BHC GRS 1758-258. However, since GRS 1758-258 sits less than 1° from the strong soft source GX 5-1, the source confusion filtering removes most of the steps from both of these sources. We have reprocessed the data with GX 5-1 classified as a weak source (class 4), assuming then that all of the > 100 keV emission is from GRS 1758-258. The 3-yr average flux for GRS 1758-258 in the 100–300 keV band is 52.6 ± 8.2 mCrab and is detected at a significance of 6.4σ .

Several other sources are at less than 5σ (including systematic errors) above 100 keV but current measurements suggest that they may reach the detection threshold as more data are accumulated. These include the AGN 3C273 (3.9σ), NGC 4151 (2.9σ), 3C454.3 (2.7σ), and NGC 2110 (2.9σ), as well as the LMXB/NS systems GS 1826-238 (4.4σ) and 1A 1742-292 (3.2σ). Either of the last two sources would be the first neutron star system detected in the GBM occultation data in the 100-300 keV energy band.

7.3. Comparisons with *Swift*/BAT

The GBM CTIME data channels 1-2 cover the 12-50 keV energy band, while *Swift*/BAT public transient monitor data⁸ spans the 15-50 keV range. As a simple check that the GBM EOT results are reasonable, we have plotted 12-50 keV GBM data for the three year interval from 2008 Aug 12 to 2011 Aug 12 along with the same time interval for *Swift*/BAT. Figure 9 shows comparisons between GBM and *Swift*/BAT data for eight representative sources. Each dataset is normalized to its own three-year average value for the Crab flux. The data are binned into 2-4 day averages but the bins are not exactly aligned in time between the two instruments. The two datasets agree quite well for these sources with the exception being Sco X-1. Because Sco X-1 has a very soft spectrum, the differing energy bands (12-50 keV for GBM and 15-50 keV for *Swift*/BAT) become important.

7.4. Transient outbursts

Figure 10 shows all transient outbursts detected to date with GBM. The time intervals for each transient outburst were defined using the flare database, described in Section 3, with the outburst time intervals defined using *Swift*/BAT data. All sources from the flare database are included in the plot, with the exception of Cyg X-1 and Cyg X-3, which are persistent sources that were listed in the flare database because they changed flux class during the course of the mission. The color bars represent outbursts with $> 5\sigma$ statistical significance in the 12-25 keV energy band, integrated over the full outburst interval. Three peak flux categories are shown: 50-150 mCrab (green), 150-500 mCrab (blue), and > 500 mCrab (red). Eight sources (V0332+53, LSV+44 17, MXB 0656-072, MAXI J1659-152, IGRJ17473-2721, EXO 1745-248, and SAX J2103.5+4545) had 3-year flux averages below our catalog detection limit in all energy bands, but were detectable at $> 5\sigma$ in the 12-25 keV band for relatively brief transient outbursts.

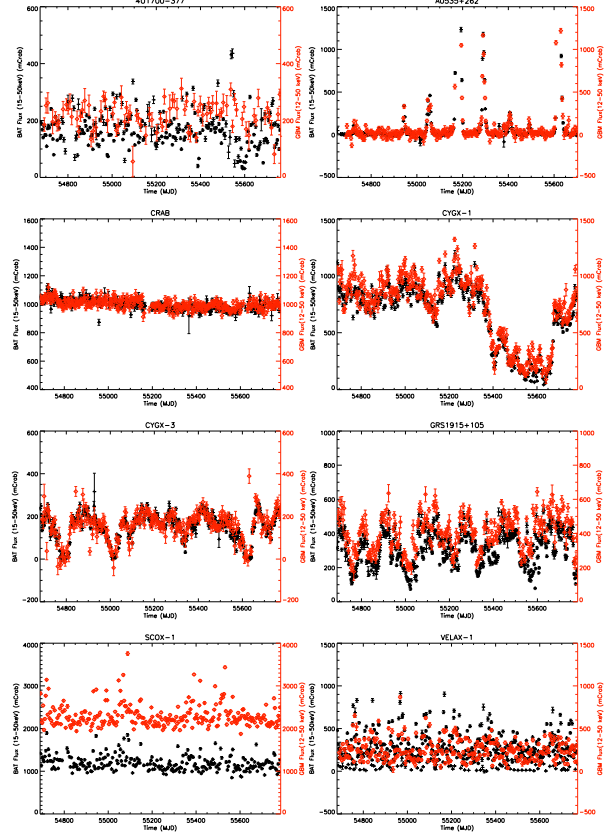


Fig. 9.— Comparisons between GBM 12-50 keV flux (diamonds) and BAT 15-50 keV flux (crosses). Plotted points are 2-4 day averages. Start and stop times for these averages are not precisely aligned between the two instruments.

GBM is able to detect flares on timescales as short as a few days and > 50 mCrab. These detections are consistent with the sensitivity plot (Figure 4) in which the 1-day sensitivity is ~ 150 mCrab in the 12-25 keV band. Thus flares with a low peak flux require a longer duration to reach the detection limit. The results from the transient source plot are consistent with this in that the outbursts that are not detected often lasted only a few days. The other outbursts not detected occurred during times when data were not available because of source confusion or no occultations. Because outbursts were added to the flare database only when the peak flux exceeded 50 mCrab in BAT, there are no events with peak fluxes less than 50 mCrab. Consequently outbursts with peak fluxes less than 50 mCrab may be detectable but have not been in-

⁸<http://swift.gsfc.nasa.gov/docs/swift/results/transients/>

that were missed by *Swift*/BAT due to solar constraints. A more detailed analysis of transient outbursts is planned for a future publication.

Table 2:: GBM Occultation Catalog Detections

Source Name	ra	dec	Category	Flux 12-25 keV (mCrabs)	Flux 25-50 keV (mCrabs)	Flux 50-100 keV (mCrabs)	Flux 100-300 keV (mCrabs)	Sig 12-50 keV (σ)	Sig 12-300 keV (σ)	Type
	(deg)	(deg)								
SUN	T	5.72 \pm 3.11	-0.03 \pm 2.84	0.76 \pm 3.28	2.15 \pm 6.13	1.4	1.1	Star
SMCX-1	19.27	-73.43	ATP	40.07 \pm 3.23	18.14 \pm 3.55	-8.97 \pm 4.30	-0.47 \pm 5.52	12.1	5.7	HMXB/NS
4U0115+634	19.63	63.74	AT	13.06 \pm 3.07	12.24 \pm 3.48	6.88 \pm 4.34	6.89 \pm 6.54	5.5	4.3	HMXB/NS
NGC1275	49.95	41.51	A	17.13 \pm 3.04	2.03 \pm 2.91	4.54 \pm 3.21	2.89 \pm 6.18	4.6	3.3	Seyfert 2
V0332+53	53.75	53.17	T	11.27 \pm 3.02	1.83 \pm 3.09	-1.52 \pm 3.60	4.11 \pm 6.07	3.0	1.9	HMXB/NS
XPER	58.85	31.05	AT	41.97 \pm 3.01	32.46 \pm 2.79	37.79 \pm 3.05	10.29 \pm 5.21	18.1	16.8	HMXB/NS
LSV+44 17	70.25	44.53	T	4.29 \pm 3.10	6.72 \pm 2.92	7.79 \pm 3.34	0.07 \pm 6.42	2.6	2.2	HMXB/NS
LMCX-4	83.20	-66.37	ATP	24.75 \pm 3.10	19.11 \pm 3.26	0.95 \pm 3.80	-8.23 \pm 5.55	9.8	4.5	HMXB/NS
CRAB	83.63	22.01	A	1000.00 \pm 3.00	1000.00 \pm 2.88	1000.00 \pm 3.05	1000.00 \pm 6.02	481.1	504.8	Pulsar/PWN
A0535+262	84.73	26.32	ATP	188.89 \pm 3.04	190.64 \pm 3.08	75.12 \pm 3.59	9.83 \pm 5.70	87.7	58.0	HMXB/NS
NGC2110	88.04	-7.46	A	12.21 \pm 3.03	15.15 \pm 2.89	15.82 \pm 3.15	17.74 \pm 6.08	6.5	7.6	Seyfert 2
4U0614+09	94.28	9.14	A	29.96 \pm 3.00	24.58 \pm 2.88	20.12 \pm 3.06	8.90 \pm 5.96	13.1	10.6	LMXB/NS
MXB0656-072	104.61	-7.26	T	3.05 \pm 2.99	-1.26 \pm 2.79	1.69 \pm 3.02	-7.59 \pm 5.04	0.4	-0.6	HMXB/NS
VELAX-1	135.53	-40.56	AP	274.83 \pm 3.03	213.39 \pm 2.94	28.06 \pm 3.29	2.53 \pm 5.53	115.7	67.4	HMXB/NS
GROJ1008-57	152.44	-58.29	T	11.77 \pm 3.09	5.60 \pm 3.12	0.47 \pm 3.62	-17.07 \pm 6.30	4.0	0.1	HMXB/NS
A1118-61	170.24	-61.92	T	15.88 \pm 3.57	4.02 \pm 4.39	-4.91 \pm 5.16	11.34 \pm 9.01	3.5	2.2	HMXB/NS
CENX-3	170.31	-60.62	AP	153.47 \pm 3.18	31.48 \pm 3.10	4.74 \pm 3.56	-5.26 \pm 5.33	41.7	23.7	HMXB/NS
1E1145.1-6141	176.87	-61.95	AP	24.27 \pm 3.22	20.19 \pm 3.53	19.29 \pm 4.33	-28.10 \pm 7.65	9.3	3.6	HMXB/NS
NGC4151	182.65	39.42	A	31.62 \pm 3.11	32.08 \pm 2.97	36.82 \pm 3.38	17.93 \pm 6.23	14.8	14.3	Seyfert 1
NGC4388	186.45	12.66	A	11.54 \pm 3.02	13.77 \pm 2.84	13.21 \pm 3.07	14.63 \pm 5.97	6.1	6.7	Seyfert 2
GX301-2	186.66	-62.77	ATP	260.11 \pm 3.25	110.28 \pm 3.19	-1.83 \pm 3.86	-13.15 \pm 6.50	81.3	40.3	HMXB/NS
3C273	187.27	2.05	A	15.31 \pm 2.99	19.75 \pm 2.86	24.30 \pm 2.99	22.56 \pm 5.84	8.5	10.6	Quasar
4U1254-690	194.40	-69.29	A	17.35 \pm 3.42	2.94 \pm 3.35	2.08 \pm 3.92	-6.57 \pm 5.04	4.2	2.0	LMXB/NS
GX304-1	195.32	-61.60	ATP	38.21 \pm 3.17	35.38 \pm 3.39	9.05 \pm 3.82	-5.52 \pm 7.20	15.8	8.2	HMXB/NS
CEN A	201.37	-43.02	A	49.92 \pm 3.06	61.50 \pm 3.03	70.40 \pm 3.23	92.69 \pm 6.19	25.9	33.5	Seyfert 2
NGC5252	204.57	4.54	A	6.54 \pm 3.03	11.62 \pm 2.86	11.87 \pm 3.10	11.54 \pm 6.02	4.4	5.2	Seyfert 2
IC4329A	207.33	-30.31	A	10.51 \pm 3.08	10.89 \pm 2.95	13.04 \pm 3.25	8.13 \pm 6.26	5.0	5.2	Seyfert 1
MAXIJ1409-619	212.01	-61.98	T	10.87 \pm 3.17	10.25 \pm 3.35	3.29 \pm 4.02	1.01 \pm 7.15	4.6	2.7	HMXB/NS
CIRCINUS GALAXY	213.29	-65.34	A	12.57 \pm 3.12	19.01 \pm 3.41	0.03 \pm 1.50	-5.87 \pm 6.51	6.8	3.2	Seyfert 2
NGC5506	213.31	-3.21	A	11.32 \pm 3.03	12.18 \pm 2.87	4.85 \pm 3.06	11.31 \pm 5.96	5.6	5.0	Seyfert 2
H1417-624	215.30	-62.70	ATP	19.95 \pm 3.17	19.44 \pm 3.24	-0.04 \pm 3.70	-9.96 \pm 7.05	8.7	3.2	HMXB/NS
CIRX-1	230.17	-57.17	T	14.13 \pm 3.44	2.31 \pm 3.09	4.04 \pm 2.81	-3.08 \pm 7.28	3.6	1.9	LMXB/NS
4U1538-52	235.60	-52.39	AP	23.62 \pm 3.10	12.97 \pm 3.19	2.89 \pm 3.41	1.20 \pm 6.37	8.2	4.8	HMXB/NS
H1608-522	243.18	-52.42	T	11.35 \pm 3.51	9.53 \pm 3.10	5.33 \pm 2.97	2.09 \pm 7.45	4.5	3.0	LMXB/NS
SCOX-1	244.98	-15.64	AP	4364.73 \pm 3.31	222.51 \pm 2.99	19.49 \pm 3.38	12.48 \pm 6.69	1028.1	529.8	LMXB/NS
X1624-490	247.01	-49.20	A	28.22 \pm 3.54	8.43 \pm 2.81	1.73 \pm 2.41	6.82 \pm 7.90	8.1	4.8	LMXB/NS
IGRJ16318-4848	247.97	-48.80	AT	39.93 \pm 3.38	39.55 \pm 3.58	4.90 \pm 4.40	1.15 \pm 8.32	16.1	8.1	HMXB/NS
AXJ1631.9-4752	248.01	-47.87	A	32.94 \pm 3.24	39.43 \pm 3.52	8.42 \pm 4.01	3.41 \pm 7.59	15.1	8.6	HMXB/NS
4U1626-67	248.07	-67.46	A	61.79 \pm 3.27	26.10 \pm 3.64	-4.62 \pm 4.58	-3.47 \pm 7.09	18.0	8.2	LMXB/NS
4U1630-472	248.50	-47.39	AT	26.76 \pm 3.22	32.90 \pm 3.48	9.15 \pm 3.90	-1.36 \pm 7.32	12.6	7.1	BHC
4U1636-536	250.23	-53.75	AT	47.15 \pm 3.49	31.88 \pm 3.98	6.34 \pm 5.09	-0.09 \pm 9.19	14.9	7.3	LMXB/NS
SWIFTJ164449.3P573451	251.20	57.60	A	12.72 \pm 3.23	13.84 \pm 3.38	3.91 \pm 4.08	-5.12 \pm 7.68	5.7	2.6	TDE
GX340+0	251.45	-45.61	A	173.17 \pm 3.63	-0.07 \pm 3.32	-6.20 \pm 4.27	-6.86 \pm 8.23	35.2	15.2	LMXB/NS
HERX-1	254.46	35.34	ATP	86.36 \pm 3.04	39.68 \pm 2.97	5.87 \pm 3.43	6.67 \pm 5.31	29.6	18.2	LMXB/NS
MAXIJ1659-152	254.76	-15.26	T	3.29 \pm 3.19	1.44 \pm 3.24	0.55 \pm 3.67	-7.14 \pm 7.11	1.0	-0.2	BHC
OAO1657-415	255.20	-41.67	AP	62.30 \pm 3.42	66.70 \pm 4.02	31.40 \pm 5.27	17.88 \pm 9.08	24.4	15.2	HMXB/NS
GX339-4	255.71	-48.79	AT	18.39 \pm 3.61	23.83 \pm 4.05	42.49 \pm 5.21	1.58 \pm 9.88	7.8	6.9	BHC
4U1700-377	255.99	-37.84	AP	230.57 \pm 3.73	209.48 \pm 4.59	112.86 \pm 6.21	20.67 \pm 10.68	74.5	41.9	HMXB/NS
GX349+2	256.45	-36.42	A	304.96 \pm 4.08	12.58 \pm 3.84	-0.22 \pm 4.03	18.63 \pm 10.20	56.7	27.3	LMXB/NS
4U1702-429	256.56	-43.04	AT	36.72 \pm 3.26	14.77 \pm 3.52	9.26 \pm 3.43	6.24 \pm 5.77	10.7	8.1	LMXB/NS
H1705-440	257.23	-44.10	AT	40.89 \pm 3.30	15.51 \pm 3.69	5.03 \pm 3.75	4.13 \pm 6.33	11.4	7.4	LMXB/NS
4U1708-407	258.10	-40.84	A	19.83 \pm 3.84	-2.96 \pm 4.44	8.12 \pm 5.84	19.46 \pm 11.16	2.9	3.2	LMXB/NS
OPH CLUSTER	258.11	-23.38	A	20.51 \pm 3.49	2.62 \pm 3.71	-4.82 \pm 4.61	-4.72 \pm 8.78	4.5	1.2	Cluster of Galaxies
GX9+9	262.93	-16.96	A	70.93 \pm 3.86	2.49 \pm 3.70	-0.75 \pm 4.53	6.68 \pm 5.74	13.7	8.8	LMXB/NS
GX354-0	263.00	-33.83	AT	87.00 \pm 3.57	53.10 \pm 3.91	20.86 \pm 4.99	-3.96 \pm 9.53	26.5	13.1	LMXB/NS
GX1+4	263.01	-24.75	AT	79.52 \pm 3.57	95.81 \pm 3.86	73.61 \pm 4.87	21.01 \pm 9.27	33.3	23.0	HMXB/NS
H1730-333	263.35	-33.39	AT	40.75 \pm 3.96	13.69 \pm 4.58	6.40 \pm 6.09	-23.93 \pm 11.56	9.0	2.6	LMXB/NS
KS1731-260	263.55	-26.09	A	38.82 \pm 4.89	27.46 \pm 4.71	21.48 \pm 5.54	15.28 \pm 13.46	9.8	6.4	LMXB/NS
SLX1735-269	264.57	-27.00	A	23.57 \pm 4.43	28.77 \pm 5.31	20.71 \pm 7.14	-9.99 \pm 13.40	7.6	3.8	LMXB/NS
X1735-444	264.74	-44.45	A	83.80 \pm 3.90	5.86 \pm 3.85	5.31 \pm 4.16	22.00 \pm 9.98	16.4	9.7	LMXB/NS
1E1740-29	265.97	-29.74	A	91.94 \pm 4.37	79.68 \pm 5.19	117.22 \pm 7.03	90.98 \pm 13.22	25.3	23.1	BHC
MAXIJ1745-288	266.46	-28.82	A	85.05 \pm 4.59	49.91 \pm 5.56	36.26 \pm 7.60	28.82 \pm 14.24	18.7	11.3	LMXB/NS

Table 2:: continued from previous page

Source Name	ra	dec	Category	Flux 12-25 keV (mCrabs)	Flux 25-50 keV (mCrabs)	Flux 50-100 keV (mCrabs)	Flux 100-300 keV (mCrabs)	Sig 12-50 keV (σ)	Sig 12-300 keV (σ)	type
	(deg)	(deg)								
1A1742-294	266.52	-29.51	A	78.37± 7.22	44.36±9.65	61.89±12.78	73.63±23.06	10.2	8.9	LMXB/NS
IGRJ17464-3213	266.58	-32.24	AT	38.54± 4.62	31.07±5.89	44.59±7.73	16.86±14.67	9.3	7.2	BHC
IGRJ17473-2721	266.83	-27.34	T	27.32± 5.62	8.04±6.95	11.99±9.74	16.80±18.42	4.0	2.8	LMXB/NS
GX3+1	266.98	-26.56	A	94.94± 4.51	7.69±4.44	-1.13±4.70	-8.96±11.95	16.2	6.5	LMXB/NS
EXO1745-248	267.23	-24.89	T	0.71± 4.42	-2.59±4.64	-5.43±6.78	9.90±12.40	-0.3	0.2	LMXB/NS
4U1746-370	267.55	-37.05	A	24.03± 3.94	3.79±4.62	7.78±6.19	18.48±11.81	4.6	3.7	LMXB/NS
XTEJ1752-223	268.04	-22.33	AT	25.98± 4.03	51.77±4.73	53.43±6.29	52.12±11.94	12.5	12.3	BHC
SWIFTJ1753.5-0127	268.37	-1.45	A	67.78± 3.46	90.51±3.87	111.28±4.95	110.43±9.09	30.5	32.8	BHC
GX5-1	270.27	-25.08	A	310.11± 12.34	30.15±17.01	-28.81±24.87	73.29±46.80	16.2	6.7	LMXB/NS
GRS1758-258	270.30	-25.73	A	65.30± 9.95	28.17±15.74	93.54±22.21	21.72±43.99	5.0	4.0	BHC
GX9+1	270.38	-20.53	A	223.96± 4.26	9.08±3.44	-0.62±4.03	-18.80±10.38	42.5	17.2	LMXB/NS
GX13+1	273.63	-17.16	A	77.54± 4.46	2.13±4.43	-3.04±4.72	11.35±12.03	12.7	6.1	LMXB/NS
4U1812-12	273.80	-12.08	A	26.80± 4.84	36.51±6.71	35.61±9.53	-7.49±17.27	7.7	4.3	LMXB/NS
GX17+2	274.01	-14.04	A	353.23± 4.38	48.03±4.52	40.39±6.06	16.99±11.58	63.7	31.6	LMXB/NS
H1820-303	275.92	-30.37	A	159.62± 3.57	15.83±4.03	-0.37±5.04	-0.62±9.12	32.6	14.9	LMXB/NS
3A1822-371	276.45	-37.10	A	49.06± 3.49	5.64±3.90	-5.13±4.69	-2.14±8.57	10.4	4.3	LMXB/NS
GS1826-238	277.37	-23.80	A	77.18± 3.40	69.19±3.82	58.57±4.74	40.42±9.24	28.6	21.2	LMXB/NS
SERX-1	279.99	5.04	A	50.29± 3.21	7.10±3.10	3.35±3.63	-8.90±5.79	12.9	6.3	LMXB/NS
SWIFTJ1842.5-1124	280.50	-11.40	T	4.18± 3.12	6.86±3.20	10.25±3.50	7.06±6.70	2.5	3.2	BHC
SWIFTJ1843.5-0343	280.90	-3.73	A	12.72± 3.19	10.25±3.18	6.01±3.69	-1.02±7.06	5.1	3.1	LMXB/NS
GS1843+00	281.41	0.89	AT	31.17± 3.10	14.84±3.21	5.86±3.76	-1.78±6.69	10.3	5.6	HMXB/NS
IGRJ18483-0311	282.08	-3.16	A	18.91± 3.18	11.99±3.16	9.05±3.65	11.66±6.99	6.9	5.7	HMXB/SFXT
HT1900.1-2455	285.04	-24.92	A	19.31± 3.09	26.65±3.09	19.92±3.50	8.04±6.69	10.5	8.5	LMXB/NS
H1907+097	287.40	9.83	A	46.21± 3.14	25.31±3.03	16.11±3.40	-2.56±4.91	16.4	11.5	HMXB/NS
4U1909+07	287.70	7.60	A	44.01± 3.17	34.83±3.27	19.95±3.91	-8.29±6.96	17.3	9.9	HMXB/NS
AQLX-1	287.82	0.58	T	6.61± 3.14	9.92±3.22	4.70±3.60	-0.19±6.93	3.7	2.3	LMXB/NS
GRS1915+105	288.82	10.97	A	540.46± 3.14	271.96±3.02	138.32±3.40	60.65±6.51	186.4	118.4	BHC
XTEJ1946+274	296.41	27.36	ATP	19.04± 3.16	10.93±3.19	4.80±3.73	-8.98±7.12	6.7	2.8	HMXB/NS
4U1954+31	298.93	32.10	AT	18.00± 3.26	15.46±3.56	3.04±4.50	-5.53±7.64	6.9	3.1	LMXB/NS
CYGX-1	299.59	35.20	AP	640.41± 3.15	779.52±3.17	944.20±3.64	881.27±6.93	317.6	360.0	BHC
EXO2030+375	308.06	37.64	ATP	29.88± 3.13	23.37±3.34	9.05±4.07	-2.26±7.40	11.6	6.2	HMXB/NS
CYGX-3	308.11	40.96	AP	196.13± 3.04	126.56±3.05	45.43±3.30	13.83±6.34	74.9	45.8	BHC
SAXJ2103.5+4545	315.90	45.76	T	5.60± 3.05	5.19±3.12	2.97±3.32	-1.37±6.21	2.5	1.5	HMXB/NS
IGRJ21247+5058	321.18	50.98	A	13.76± 3.19	10.93±3.29	8.20±3.95	6.78±7.50	5.4	4.1	Radio Galaxy
GINGA2138+56	324.88	56.99	T	9.15± 3.18	7.42±3.28	-1.60±4.02	-1.44±6.33	3.6	1.5	HMXB/NS
CYGX-2	326.17	38.32	A	138.01± 3.10	14.04±2.85	-2.24±3.08	5.60±5.97	36.1	19.6	LMXB/NS
3C454.3	343.49	16.15	A	5.57± 2.95	6.19±2.78	11.73±2.76	14.56±5.32	2.9	5.3	Quasar

Table 3:: GBM Occultation Catalog Marginal Detections

Source Name	ra	dec	Category	Flux 12-25 keV (mCrabs)	Flux 25-50 keV (mCrabs)	Flux 50-100 keV (mCrabs)	Flux 100-300 keV (mCrabs)	Sig 12-50 keV (σ)	Sig 12-300 keV (σ)	Type
	(deg)	(deg)								
3A0114+650	19.51	65.29	B	12.96± 3.15	5.66±3.39	10.81±4.18	14.41±7.16	4.0	4.6	HMXB/NS
GKPER	52.80	43.90	B	8.58± 3.05	6.75±2.96	-1.20±3.28	6.67±6.34	3.6	2.5	CV
LMCX-3	84.79	-64.08	B	12.36± 3.18	8.76±3.27	9.08±3.84	-4.86±7.20	4.6	2.7	BHC
VELA-X	128.29	-45.19	B	12.42± 3.12	6.38±3.11	12.16±3.57	6.32±6.78	4.3	4.2	Pulsar/PWN
VELA PSR	128.85	-45.18	B	12.80± 3.06	7.40±3.12	8.83±3.44	6.54±6.59	4.6	4.1	Pulsar/PWN
MCG-05-23-016	146.92	-30.95	B	7.86± 3.06	9.69±2.95	4.40±3.25	4.09±6.21	4.1	3.2	Seyfert 2
1FGLJ1018.6-5856	154.73	-58.95	B	7.21± 3.16	12.63±3.19	-5.93±3.68	3.18±6.93	4.4	1.9	Gamma Ray Binary
MRK421	166.11	38.21	B	11.24± 3.01	4.59±2.71	6.58±3.14	5.39±6.08	3.9	3.5	BL Lac - type object
NGC3783	174.75	-37.73	B	7.35± 3.09	11.67±3.00	2.44±3.36	-5.90±6.43	4.4	1.8	Seyfert 1
COMA CLUSTER	194.95	27.98	B	11.47± 3.02	8.93±2.85	1.24±3.09	-5.56±5.97	4.9	2.0	Cluster of Galaxies
4U1323-62	201.65	-62.14	B	15.42± 3.27	6.72±3.42	8.99±4.10	-8.09±7.73	4.7	2.3	LMXB/NS
MSH15-52	228.51	-59.26	B	2.13± 3.24	10.09±3.32	13.85±3.92	8.01±7.40	2.6	3.6	Pulsar/PWN
H 1517+656	229.45	65.42	B	7.73± 3.23	7.62±3.47	3.70±4.18	-4.39±7.90	3.2	1.4	BL Lac - type object
IGRJ16418-4532	250.45	-45.53	B	17.46± 3.67	4.13±4.06	-4.30±5.18	-2.56±9.76	3.9	1.2	HMXB/SFXT

Table 3:: continued from previous page

Source Name	ra	dec	Category	Flux 12-25 keV (mCrabs)	Flux 25-50 keV (mCrabs)	Flux 50-100 keV (mCrabs)	Flux 100-300 keV (mCrabs)	Sig 12-50 keV (σ)	Sig 12-300 keV (σ)	type
	(deg)	(deg)								
TXS 1700+685	255.04	68.50	B	10.09 \pm 3.21	6.93 \pm 3.60	3.32 \pm 4.17	-3.92 \pm 7.73	3.5	1.6	Seyfert 1
GRS1724-308	261.90	-30.80	B	13.86 \pm 3.82	14.19 \pm 4.31	-0.56 \pm 5.64	-5.91 \pm 10.67	4.9	1.6	LMXB/NS
B2 1732+38A	263.59	38.96	B	2.50 \pm 3.04	2.38 \pm 3.05	9.79 \pm 3.25	-4.15 \pm 6.22	1.1	1.3	BL Lac - type object
SAXJ1806.5-2215	271.64	-22.24	B	18.21 \pm 4.09	1.80 \pm 4.91	5.85 \pm 6.66	14.30 \pm 12.74	3.1	2.6	LMXB/NS
SAXJ1818.6-1703	274.66	-17.05	B	14.13 \pm 4.22	5.66 \pm 4.95	-3.01 \pm 6.63	4.14 \pm 12.74	3.0	1.3	HMXB/SFXT
XTEJ1855-026	283.88	-2.61	B	14.11 \pm 3.17	7.56 \pm 3.14	2.02 \pm 3.63	-0.45 \pm 6.96	4.9	2.6	HMXB/NS
4U2127+119	322.49	12.17	B	6.12 \pm 3.05	7.68 \pm 2.90	7.69 \pm 3.18	1.57 \pm 6.14	3.3	2.8	LMXB/NS
4U2206+54	331.98	54.52	B	8.81 \pm 3.15	9.67 \pm 3.32	8.22 \pm 3.97	6.18 \pm 7.48	4.0	3.4	HMXB/NS
CAS A	350.86	58.82	B	7.35 \pm 3.15	8.92 \pm 3.21	2.20 \pm 3.81	15.52 \pm 7.22	3.6	3.6	SNR

Table 4:: GBM Occultation Catalog Upper Limits

Source Name	ra	dec	Category	< Flux (3σ) 12-25 keV (mCrabs)	< Flux (3σ) 25-50 keV (mCrabs)	< Flux (3σ) 50-100 keV (mCrabs)	< Flux (3σ) 100-300 keV (mCrabs)	Type
	(deg)	(deg)						
IGR J00234+6141	5.74	61.69	N	9.51	9.78	11.70	22.20	CV
V709 CAS	7.20	59.29	N	9.45	9.60	11.37	21.57	CV
BD+6270	9.30	61.38	N	9.48	9.75	11.61	22.05	Star
FERMIJ0109+6134	17.44	61.56	N	9.12	9.39	9.96	18.30	Blazar
PKS 0116-219	19.74	-21.69	N	8.85	8.34	8.31	16.08	Quasar
PKS 0142-278	26.26	-27.56	N	8.85	8.40	8.43	16.26	Quasar
PKS 0215+015	34.45	1.75	N	8.82	8.28	8.22	15.87	Quasar
S4 0218+35	35.27	35.94	N	8.85	8.40	8.40	16.17	Quasar
PKS 0235-618	39.22	-61.60	N	9.15	9.36	10.08	18.96	Quasar
LSI+61 303	40.13	61.23	N	9.18	9.48	10.47	19.86	Gamma Ray Binary
PKS 0244-470	41.50	-46.86	N	9.00	8.91	9.30	17.76	Quasar
ALGOL	47.04	40.96	N	9.09	8.64	9.48	18.24	Star
PKS 0332-403	53.56	-40.14	N	9.06	8.79	9.57	18.57	BL Lac - type object
PKS 0347-211	57.49	-21.05	N	8.85	8.43	8.46	16.29	Quasar
PKS 0402-362	60.97	-36.08	N	8.91	8.61	8.85	16.95	Quasar
PKS 0420-01	65.82	-1.34	N	8.85	8.37	8.34	16.11	Quasar
PKS 0440-00	70.66	-0.30	N	8.88	8.49	8.55	16.44	Quasar
3C129	72.29	45.01	N	9.21	8.97	10.14	19.47	Quasar
LMCX-2	80.12	-71.96	N	9.75	10.20	12.24	22.86	LMXB/NS
PKS 0528+134	82.74	13.53	N	9.09	8.97	9.69	18.78	Quasar
MAXIJ0556-332	89.19	-33.17	N	9.12	8.79	9.69	18.60	LMXB/NS
PKS 0601-70	90.30	-70.60	N	9.33	9.81	10.77	20.01	Quasar
TXS 0628-240	97.75	-24.11	N	9.06	8.76	9.48	18.39	BL Lac - type object
HESSJ0632+057	98.25	5.80	N	9.06	8.52	9.21	17.79	Gamma Ray Binary
MG2 J071354+193	108.48	19.58	N	8.85	8.37	8.37	16.14	Blazar
4C +14.23	111.32	14.42	N	8.85	8.37	8.37	16.17	Quasar
PKS 0805-07	122.06	-7.85	N	8.88	8.49	8.55	16.47	Quasar
BZQ J0850-1213	132.54	-12.23	N	8.91	8.58	8.70	16.74	Quasar
S4 0917+44	140.24	44.70	N	9.00	8.85	9.24	17.64	Quasar
4C +55.17	149.41	55.38	N	9.09	9.24	9.93	18.78	Quasar
MG2 J101241+243	153.17	24.66	N	8.88	8.43	8.49	16.38	Quasar
TXS 1013+054	154.01	5.22	N	8.88	8.52	8.61	16.62	Quasar
FIRSTJ102347.6+003841	155.95	0.64	N	9.06	8.55	9.24	17.91	LMXB/NS
PKS 1124-186	171.77	-18.96	N	8.94	8.58	8.70	16.77	Quasar
TON 599	179.88	29.25	N	8.91	8.52	8.64	16.65	Quasar
1FGLJ1227.9-4852	186.98	-48.88	N	9.57	9.72	11.31	21.42	Pulsar/PWN
PKS 1244-255	191.70	-25.80	N	9.00	8.73	8.94	17.13	Quasar
3C 279	194.05	-5.79	N	8.94	8.58	8.70	16.80	Quasar
PSRB1259-63	195.70	-63.83	N	9.54	10.41	11.49	21.15	Pulsar/PWN
GB 1310+487	198.18	48.48	N	9.03	9.03	9.57	18.18	Quasar
PKS 1329-049	203.02	-5.16	N	8.94	8.55	8.64	16.71	Quasar
CENX-4	224.59	-31.67	N	9.03	8.67	8.82	16.89	LMXB/NS

Table 4:: continued from previous page

Source Name	ra	dec	Category	Flux (3σ) 12-25 keV (mCrabs)	Flux (3σ) 25-50 keV (mCrabs)	Flux (3σ) 50-100 keV (mCrabs)	Flux (3σ) 100-300 keV (mCrabs)	type
	(deg)	(deg)						
PKS 1502+106	226.10	10.49	N	8.97	8.61	8.76	16.86	Quasar
PKS 1510-08	228.21	-9.10	N	9.00	8.58	8.70	16.71	Quasar
B2 1520+31	230.54	31.74	N	9.00	8.82	9.18	17.67	Quasar
SWIFT J1539.2-6227	234.82	-62.46	N	9.42	9.84	10.89	20.61	BHC
4U1543-624	236.98	-62.57	N	9.90	10.32	12.45	23.52	LMXB/NS
SGR1550-5418	237.73	-54.31	N	9.36	9.93	11.70	21.69	SGR
PKS 1551+130	238.39	12.95	N	9.06	8.88	9.24	17.79	Quasar
USCO	245.63	-17.88	N	10.14	10.56	12.96	24.99	CV
PKS 1622-253	246.45	-25.46	I	9.36	9.57	10.41	19.89	Quasar
4C +38.41	248.81	38.13	N	9.09	9.12	9.75	18.66	Quasar
IGRJ16479-4514	251.98	-45.23	N	12.66	15.30	20.52	38.40	HMXB/SFXT
GROJ1655-40	253.50	-39.85	I	10.89	12.12	15.54	29.61	BHC
XTEJ1701-462	255.24	-46.19	I	11.34	13.08	17.13	32.43	LMXB/NS
IGRJ17091-3624	257.27	-36.40	N	11.40	12.96	16.95	32.61	BHC
SWIFT J1713.4-4219	258.36	-42.33	N	10.83	13.11	16.17	30.84	BHC
4C +51.37	265.15	52.20	N	9.27	9.72	10.71	20.19	Quasar
NGC6440	267.22	-20.36	N	11.40	12.90	16.83	32.07	Globular Cluster
HESS J1825-137	276.13	-13.85	N	10.38	11.13	13.89	26.49	Pulsar/PWN
4U1822-000	276.34	-0.01	N	9.75	9.87	11.73	22.47	LMXB/NS
LS5039	276.56	-14.85	N	10.35	11.10	13.86	26.43	Gamma Ray Binary
SGR1833-0832	278.43	-8.52	N	9.90	10.20	12.24	23.40	SGR
MAXIJ1836-194	278.96	-19.39	I	10.05	10.98	13.14	25.23	BHC
S4 1849+67	282.32	67.09	N	9.69	10.95	12.72	23.67	Seyfert 1
S4 1851+48	283.12	48.93	N	9.69	10.95	12.72	23.67	Quasar
IGRJ18539+0727	283.48	7.46	I	9.30	9.57	10.41	19.71	BHC
XTEJ1858+034	284.65	3.35	I	9.45	9.54	10.35	14.52	HMXB/NS
TXS 1902+556	285.80	55.68	N	9.72	10.44	12.57	23.94	BL Lac - type object
4U1901+03	285.90	3.19	I	9.81	10.02	11.55	15.48	HMXB/NS
TXS 1920-211	290.88	-21.08	N	9.06	8.76	9.00	17.28	Quasar
IGRJ19294+1816	292.48	18.64	N	9.15	9.30	9.75	18.06	HMXB/SFXT
PKS 1954-388	299.50	-38.75	N	9.06	8.82	9.12	17.43	Quasar
4U1957+115	299.85	11.71	N	9.24	8.88	9.84	18.93	LMXB/NS
PKS 2052-47	314.07	-47.25	N	9.12	9.09	9.57	18.27	Quasar
V407CYG	315.54	45.78	N	9.51	9.69	11.46	21.90	CV
SS CYG	325.68	43.59	N	9.51	9.60	11.43	21.72	CV
OX 169	325.90	17.73	N	8.94	8.61	8.76	16.83	Seyfert 1
PKS 2155-304	329.72	-30.23	N	9.06	8.67	9.27	18.06	BL Lac - type object
PKS 2201+171	330.86	17.43	N	8.91	8.52	8.61	16.56	Quasar
CTA 102	338.15	11.73	N	8.94	8.49	8.76	17.13	Quasar
PKS 2255-282	344.52	-27.97	N	8.88	8.46	8.58	16.56	Seyfert 1
B2 2308+34	347.77	34.42	N	8.88	8.43	8.49	16.29	Quasar
CTS 0490	351.37	-35.97	N	8.88	8.52	8.61	16.62	Quasar
PKS 2325+093	351.89	9.67	N	8.82	8.28	8.22	15.90	Quasar
PKS 2326-502	352.34	-49.93	N	9.03	9.00	9.45	18.03	Quasar
PMN J2345-1555	356.30	-15.92	N	8.85	8.34	8.31	16.05	Quasar

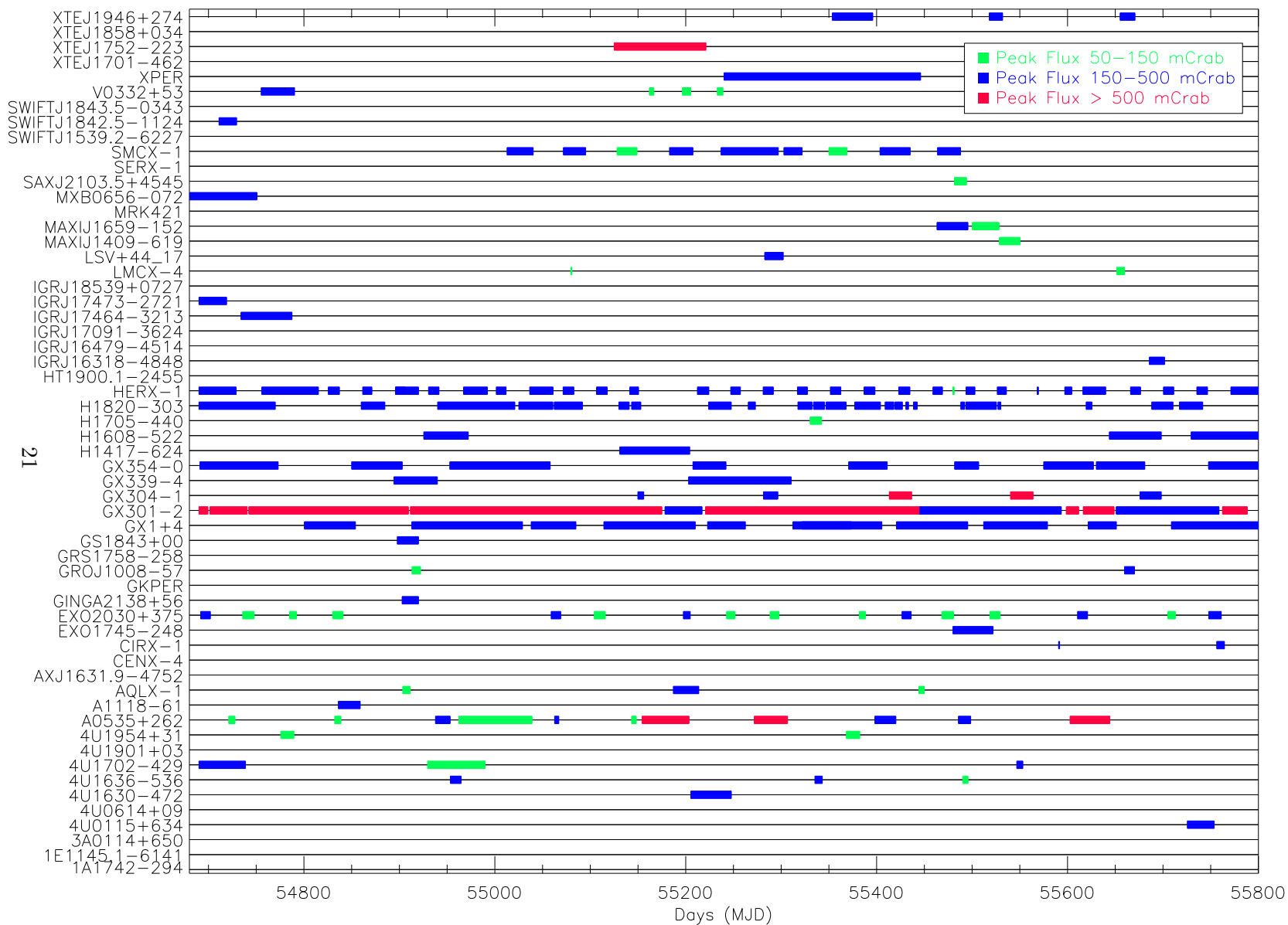


Fig. 10.— Bar plot of transient outbursts detected with GBM.

7.5. Periodicity Analysis

Using three years of continuous data from GBM, we have produced folded light curves and performed searches for periodicities for all the X-ray binary systems monitored with the Earth occultation technique. For purposes of this catalog, this analysis is intended to increase the confidence of source detections presented in Table 2.

For this simple approach, the lightcurves were folded without barycentering. Values in each phase bin were calculated using weighted averages and statistical (counting) errors, which do not account for intrinsic variability of the source flux. Our primary detection criteria uses a $\Delta\chi^2$ fit of the folded light curve, at the known orbital period, to a constant average flux. Our initial cut considered an orbital period detected when $\Delta\chi^2 > 40$ for 10 degrees of freedom and the statistical chance probability is $< 1 \times 10^{-5}$. To estimate systematic effects, we folded the data for 3C 279, an undetected source not expected to show periodicities, at each of the known periods for which we were folding data. The maximum $\Delta\chi^2$ found for 3C 279 was 80 for a period of 18.5 days. Therefore our final detection criteria for orbital periods were $\Delta\chi^2 > 80$ for 10 degrees of freedom, corresponding to a statistical chance probability of 5×10^{-13} . Table 5 lists the detected sources, known orbital periods, $\Delta\chi^2$ value, and references for each orbital period. A total of 18 sources were detected, of which 14 are HMXB/NS and two are LMXB/NS systems, and two BH systems. The detectable orbital periods ranged from minutes to hundreds of days. Figure 11 shows the orbital light curves in the 12–50 keV band for a sample of binaries: the microquasar Cyg X–3, the black hole system Cyg X–1, the wind-fed HMXBs 4U 1538–52 and GX 301–2, and the Be/X-ray binaries EXO 2030+375 and XTE J1946+274. Arbitrary orbital phases are plotted.

We also attempted a more ambitious periodicity search. Since our data are unevenly sampled, the Lomb-Scargle periodogram (Scargle 1982) is better suited to the GBM data than a direct Fourier transform technique. However the non-sinusoidal nature and red-noise in many of

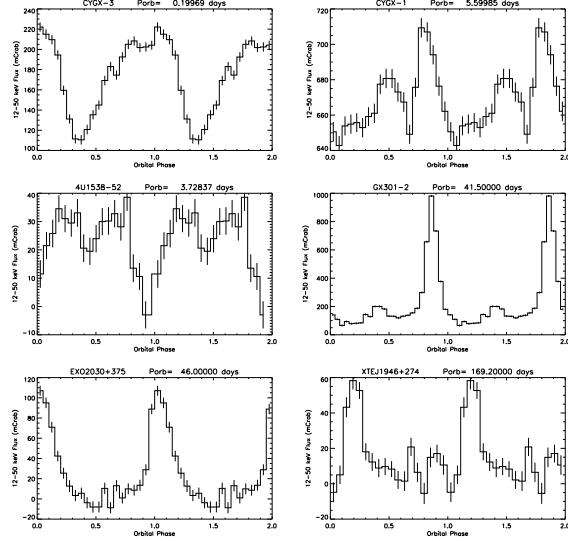


Fig. 11.— Orbital light curves in the 12–50 keV band for a sample of binaries detected by GBM using EOT. The sample includes the microquasar Cyg X–3, the black hole system Cyg X–1, the wind-fed HMXRBs 4U 1538–52 and GX 301–2, as well as the Be/X-ray binaries EXO 2030+375 and XTE J1946+274. Arbitrary orbital phases are plotted.

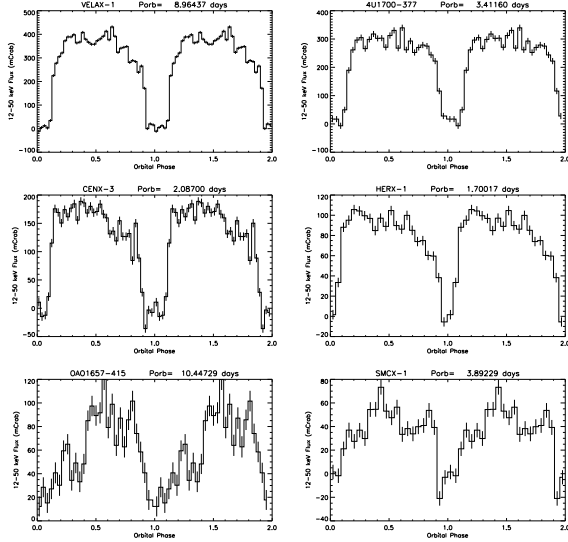


Fig. 12.— Eclipse profiles in the 12–50 keV band for 6 bright persistent HMXBs: Vela X–1, 4U 1700–377, Cen X–3, Her X–1, OAO 1657–415 and SMC X–1.

the light curves resulted in only eight sources being easily detected using the Lomb-Scargle

TABLE 5
ORBITAL PERIODS OBSERVED IN GBM EOT LIGHT CURVES

Name	type	Known Porb (days)	$\Delta\chi^2$ (dof=10)	Reference
CYGX-3	HMXB/BH	0.19969	1159.42	Singh et al. (2002)
SCOX-1	LMXB/NS	0.78700	1007.48	Cowley & Crampton (1975)
LMCX-4	HMXB/NS	1.40804	95.62	Levine, Rappaport, & Zojcheski (2000)
HERX-1	LMXB/NS	1.70017	926.97	Wilson, Scott, & Finger (1997)
CENX-3	HMXB/NS	2.08700	2907.21	Finger et al. (2010)
4U1700-377	HMXB/NS	3.41159	2490.47	Finger (2012a)
4U1538-52	HMXB/NS	3.72836	120.00	Finger (2012b)
SMCX-1	HMXB/NS	3.89229	220.00	Wojdowski et al. (1998)
CYGX-1	HMXB/BH	5.59985	210.58	Iorio (2008)
VELAX-1	HMXB/NS	8.96436	20222.78	van Kerkwijk et al. (1995)
OA01657-415	HMXB/NS	10.44750	269.32	Jenke et al. (2012)
1E1145.1-6141	HMXB/NS	14.36500	145.04	Ray & Chakrabarty (2002)
GX301-2	HMXB/NS	41.50000	23760.50	Koh et al. (1997)
H1417-624	HMXB/NS	42.12000	141.92	Liu, van Paradijs, & van den Heuvel (2006)
EXO2030+375	HMXB/NS	46.00000	819.78	Wilson, Finger, & Camero-Arranz (2008)
A0535+262	HMXB/NS	111.00000	88381.29	Bildsten et al. (1997)
GX304-1	HMXB/NS	133.00000	5296.86	Priedhorsky & Terrell (1983)
XTEJ1946+274	HMXB/NS	169.20000	193.63	Wilson et al. (2003)

technique. These bright and frequently active sources included the microquasar Cyg X-3 and 7 HMXB/NS systems: 4U 1700-377, A0535+262, Cen X-3, EXO 2030+375, GX 301-2, GX 304-1, and Her X-1. Because our goal for this initial catalog was confirmation of detections, we did not pursue this analysis further.

Several bright X-ray binaries containing neutron stars undergo complete eclipses by their companions. In Fig 12 we present eclipse profiles in the 12–50 keV band for 6 bright persistent HMXBs: Vela X-1, 4U 1700-377, Cen X-3, Her X-1, OA01657-415 and SMC X-1. As described in section 3, during the fitting process eclipsing sources are excluded as interfering source terms when they are in eclipse as defined by the the eclipse database. These sources were strong detections (Table 5) using the folded orbit profiles. Three of these sources were also easily detected using Lomb-Scargle techniques.

8. Summary and Future Plans

During the first three years of the *Fermi* mission, from 2008 August 12 to 2011 August 11, we monitored a catalog of 209 sources using the Earth occultation technique. A total of 99 sources were detected at $> 5\sigma$ (including sys-

tematic errors) in 3-year average fluxes or via transient or periodicity searches. X-ray binaries containing neutron stars dominated the detected sources with 40 of 52 monitored LMXB/NS systems and 31 of 39 monitored HMXB/NS systems. Black hole systems (BHC) were the next most numerous class detected, with 12 detections out of 19 monitored, including seven detected in the 100-300 keV band and one in the 300-500 keV band. Twelve AGN sources of 71 monitored were detected, with one of these detected in the 100-300 keV 3-year average flux. Five additional AGN sources and two LMXB/NS look promising for detection above 100 keV with more data. All-sky monitoring with the GBM EOT complements other sky monitoring instrument, providing confirming observations below 100 keV, providing coverage when other instruments are limited by solar constraints, and providing important monitoring observations above 100 keV, to reveal e.g. state changes in BHC such as Cyg X-1 and XTE J1752-223. Future work using the BGO detectors with custom CSPEC data above 100 keV will provide additional effective area in the 100-500 keV band and will explore energies above 1 MeV for bright events. Multi-instrument monitoring including GBM was crucial to our discov-

ery of the 7% decline of the Crab Nebula flux from 2008-2010 (Wilson-Hodge et al. 2011a).

This work is supported by the NASA *Fermi* Guest Investigator program, NASA/Louisiana Board of Regents Cooperative Agreement NNX07AT62A (LSU), and the Louisiana Board of Regents Graduate Fellowship Program (J. Rodi). We thank the NOAA Space Prediction Center helpdesk for their support and Sebastian Drave for providing information about SFXT systems with known orbital solutions. Flare database entries and *Swift*/BAT comparisons relied upon *Swift*/BAT transient monitor results provided by the *Swift*/BAT team. This research has made use of the *MAXI* data provided by RIKEN, JAXA and the *MAXI* team and results provided by the *RXTE*/ASM teams at MIT and GSFC.

REFERENCES

- Abdo, A.A. et al. 2011, arXiv:1108.1435v1
Ackermann, M. et al. 2011a, arXiv:1108.1420v2
Ackermann, M. et al. 2011b, ApJ, accepted, arXiv:1111.7026v1
Baumgartner, W. et al. 2010, ApJS, submitted; and <http://swift.gsfc.nasa.gov/docs/swift/results/bs58mon/>
Bildsten, L. et al. 1997, ApJS, 113, 367
Bissaldi, E. et al. 2009, Exp. Astron., 24, 47
Bowyer, S., Byram, E.T., Chubb, T.A., & Friedman, H. 1964, Science, 146, 912
Camero-Arranz, A. et al. ApJ, submitted, arXiv:1109.3924
Case, G.L. et al. 2011a, ApJ, 729, 105
Case, G. L., Wilson-Hodge, C. A., Camero-Arranz, A., Chaplin, V., Cherry, M. L., Finger, M., & Jenke, P. 2011b, ATel # 3636
Case, G. L., Wilson-Hodge, C. A., Camero-Arranz, A., Chaplin, V., Cherry, M. L., Finger, M., & Jenke, P. 2011c, ATel # 3802
Case, G.L. et al. 2011d, in Proc. 2011 Fermi Symposium, eConf C110509, arXiv:1111.0686
Case, G.L. et al. 2012, in preparation
Cowley, A. P., & Crampton, D. 1975, ApJ, 201, L65
Davidson, P.J.N & Morrison, L.V 1977, MNRAS, 178, 53
Finger, M.H., Wilson-Hodge, C.A, Camero-Arranz, A., Jenke, P. 2010, BAAS, 41, 726
Finger, M.H. 2012a, in preparation
Finger, M.H. 2012b, in preparation
Fukada et al. 1975, Nature, 255, 465
Grinberg, V. et al. 2011, ATel # 3534
Harmon, B. A. et al. 2002, ApJS, 138, 149
Harmon, B. A. et al. 2004, ApJS, 154, 585
Hoover, A. S. et al. 2008, in Gamma-Ray Bursts 2007 (AIP Conf. Proc. 1000), ed. M. Galassi, D. Palmer, & E. Fenimore (Melville, NY:AIP), 565
Iorio, L., 2008, Ap&SS, 315, 335
Jenke, P., Finger, M.H., Wilson-Hodge, C.A., Camero-Arranz, A. 2012, ApJ, submitted
Jourdain, E. & Roques, J.P. 2009, ApJ, 704, 17
Koh, D. T., Bildsten, L., Chakrabarty, D., Nelson, R. W., Prince, T. A., Vaughan, B. A., Finger, M. H., Wilson, R. B., Rubin, B. C., 1997, ApJ, 479, 933
Krivonos, R. et al. 2010, A&A, 523, A61
Levine, A.M. et al. 1996, 469, L33
Levine, A. M., Rappaport, S. A., & Zojcheski, G. 2000, ApJ, 541, 194
Ling, J. C. et al. 2000, ApJS, 127, 79
Matsuoka, M. et al. 2009, PASJ, 61, 999
Liu, Q. Z., van Paradijs, J., & van den Heuvel, E. P. J. 2006, A&A, 455, 1165
Meegan, C. et al. 2009, ApJ, 702, 791
Negoro, H. et al. 2010, # ATel 2711
Negoro, H. et al. 2011, # ATel 3534
Nowak, M. A. et al. 2011, ApJ, 728, 13
Priedhorsky, W.C. & Terrell, J., 1983, ApJ, 273, 709
Ray, P.S. & Chakrabarty, D. 2002, ApJ, 581, 1293
Rodi, J. et al. 2011, in 2011 Fermi Symposium Proceedings, eConf C110509, arXiv:1111.0345
Rushton, A. et al. 2010, ATel 2714
Quiroz, R.S. 1961, J. Geophys. Res., 66, 2129
Scargle, J.D. 1982, ApJ, 263, 835
Singh, N.S, Naik, S., Paul, B., Agrawal, P. C., Rao, A. R., Singh, K. Y. 2002, A&A, 392, 161
Stella, L., White, N. E., Davelaar, J., Parmar, A. N., Blissett, R. J., & van der Klis, M. 1985, ApJ, 288, L45
Toor, A., & Seward, F. D. 1974, AJ, 79, 995
US Committee on Extension to the Standard Atmosphere 1976, US Standard Atmosphere, NOAA-S/T 76-1562 (Washington, DC:U.S. Govt Printing Office)
Van Kerkwijk M.H., van Paradijs J., Zuiderwijk E.J., et al., 1995, A&A 303, 483
Wilson, C.A., Finger, M.H., Camero-Arranz, A., 2008, ApJ, 678, 1268
Wilson, C. A., Finger, M. H., Coe, M. J. and Negueruela, I., 2003, ApJ, 584, 996
Wilson, R.B., Scott, D.M., & Finger, M.H. 1997 in The Fourth Compton Symposium, AIP conference proceedings 410, 739
Wilson-Hodge, C.A. & Case, G.L. 2010, ATel # 2721
Wilson-Hodge, C.A. et al. 2011a, ApJ, 729, 105
Wilson-Hodge, C.A. et al. 2011b, PoS(HTRS 2011)043, <http://pos.sissa.it/>
Wodjowski, P. et al. 1998, ApJ, 502, 253

This 2-column preprint was prepared with the AAS L^AT_EX macros v5.2.